



Master of Science Thesis

A Physical X-Ray Scintillator Detector Model for CBCT Imaging Applications

Mikael Kördel
mkordel@kth.se

June 19, 2014

Medical Imaging at KTH
Elekta Instrument AB
Supervisors: Markus Eriksson, Elekta & Hans Bornefalk, KTH
Examiner: Mats Danielsson, KTH

TRITA-FYS 2014:48
ISSN 0280-316X
ISRN KTH/ FYS/ -14:48-SE

Abstract

A comprehensive physical model has been developed, characterizing the response of a Thales Pixum CBCT 2630 X-ray detector, for CBCT imaging applications. The model takes into account both the spread of the signal, across adjacent pixels, and the temporal characteristics of the detector, causing residual images in subsequent projections as well as a change in sensitivity due to previous exposure.

The studied detector belongs to the category of indirect flat panel detectors, utilizing a thallium doped caesium iodide (CsI:Tl) scintillator to convert the incident X-rays into optical photons, which are detected using hydrogenated amorphous silicon (a-Si:H) photodiodes. The spatial spread of the response is due to the transport of optical photons in the scintillator, and is here described by the energy- and angle-dependent point spread function. The temporal response is characterized by the closely related effects of image lag and ghosting, which both depend on charge trapping in the amorphous silicon. These effects are modelled and tested individually.

The derived models have been compared with the results of numerous experiments and have thereby been fitted to describe the specifically studied detector. The general analytical results and presented experimental methods can be used in order to model the response of similar flat panel X-ray detectors.

Referat

En fysikalisk röntgendetektormodell för tillämpningar inom datortomografi

En omfattande fysikalisk modell, som karakteriseras med responsen hos en Thales Pixum CBCT 2630 röntgendetektor, har utvecklats för användning inom datortomografi. Modellen tar både hänsyn till spridningen av signalen över närliggande pixlar och detektorns temporala egenskaper, vilka orsakar kvarliggande skuggbilder i efterföljande projektioner samt en ändring i känslighet till följd av tidigare exponering.

Den undersökta detektorn tillhör kategorin indirekta digitala röntgendetektorer och använder sig av en scintillator av talliumdopad cesiumjodid (CsI:Tl), för att omvandla de infallande röntgenstrålarna till optiska fotoner. Dessa detekteras sedan och omvandlas till elektrisk ström i fotodioder av amorft kisel (a-Si). Den rumsliga spridningen av detektorresponsen beror på transporten av de optiska fotonerna genom scintillatoren. Detta beskrivs genom den energi- och vinkelberoende punktspridningsfunktionen. Tidsberoendet hos detektorresponsen karakteriseras av två nära besläktade fenomen, som kallas image lag och ghosting. Båda dessa effekter grundar sig på ett fenomen som kallas charge trapping, vilket innebär att laddningsbärare i kiseldioderna under en begränsad tid fastnar i metastabila energitillstånd i kislets bandstruktur.

Genom jämförelser med ett stort antal experiment har de härledda modellerna anpassats till att beskriva den undersökta detektorn. De allmänna analytiska resultaten och de experimentella metoderna kan användas för att modellera responsen hos liknande digitala röntgendetektorer.

Acknowledgements

I would like to thank my supervisors and colleagues at Elekta for providing the opportunity to work with cutting-edge medical technology. My appreciation especially goes to Markus Eriksson, Håkan Nordström and Jonas Adler for their expertise and creativity, as well as their encouragement and genuine interest in my work. My thanks also goes to my supervisors Hans Bornefalk and Mats Danielsson, of the Medical Imaging research group at KTH.

Finally, I would like to extend my admiration to Markus Eriksson and Björn Nutti for their patient and persistent work with a, not always properly functioning, CBCT scanner.

Contents

Abstract	iii
Referat	iv
Acknowledgements	v
Contents	vi
1 Introduction	1
1.1 Cone Beam Computed Tomography	1
1.2 Image Correction	3
1.3 Problem Specification	4
1.4 Layout of thesis	4
2 Background	5
2.1 Electromagnetic Radiation and X-Rays	5
2.2 X-ray Matter Interaction	8
2.3 Electronic Band Structure	11
2.4 Digital X-ray Detectors	13
2.5 Monte Carlo Methods	14
3 Flat Panel Scintillator X-ray Detector	15
3.1 Scintillator	15
3.2 Active Matrix Array	20
3.3 Photodiode Sensing Element	22
3.4 Modelling the Detector Response	25
4 Point Spread Function	27
4.1 An Analytical Model of the Scintillator Response	27
4.2 Modifications and Simplifications	32
5 Temporal Characteristics of the Detector	33
5.1 Image Lag	33
5.2 Ghosting	39

5.3	Modelling the Temporal Response	40
6	Experimental Methods	43
6.1	Detector Set-up and Limitations	43
6.2	Measuring the Point Spread Function	46
6.3	Measuring the Temporal Response	49
7	Results	55
7.1	The Point Spread Function	55
7.2	Image Lag	58
7.3	Ghosting	61
7.4	Correction for Image Lag and Ghosting	62
8	Discussion	69
8.1	The Scintillator Thickness	69
8.2	The Point Spread Function	70
8.3	The Temporal Response	70
8.4	Some Notes on the Experimental Data	71
8.5	Image Correction	72
9	Conclusion	73
	Bibliography	75

1 | Introduction

Medical X-ray imaging has been used under clinical conditions for more than a hundred years. After Wilhelm Röntgen began to study X-rays, in 1895, it did not take more than a few months before they were first used in the context of surgical operation. Since then, research has been focused on achieving higher contrast and spatial resolution, as well as increased speed and efficiency.

The thesis work presented here was done at Elekta Instrument AB, a medical technology company, mainly focused on radiotherapy and non-invasive radiosurgery. In the context of any radiation treatment, detailed imaging of the patient is needed. The images are used for diagnostic purposes, as well as in treatment planning and patient positioning. For the latter application, in the context of radiosurgery, Elekta is currently developing a complete *cone beam computed tomography* (CBCT) solution. An important part of the CBCT is a flat panel X-ray detector, in this particular case a Pixum CBCT 2630, manufactured by Thales Electron Devices.

The objective has been to develop a detailed physical model of the X-ray detector response. The model may be used in various applications, to improve the image quality of the CBCT.

1.1 Cone Beam Computed Tomography

Cone beam computed tomography (CBCT) is a computer assisted imaging technique that uses a large number of X-ray projection images, in order to reconstruct a 3D geometry. It is mainly used in medical applications, such as dentistry and image guided radiotherapy. The required set of images is obtained during a rotation of the CBCT scanner around the patient, resulting in projections at a range of different angles. A reconstruction algorithm then uses the data from the scan to produce tomographic images, i.e., thin virtual slices, which together form the 3D geometry.

In CBCT, the X-rays from the source are divergent, forming a conical shape. The source can, in many cases, be considered as a point source, while the projection onto the detector is at least as large as the projected volume. An illustration of the CBCT scanner and its relevant parts is shown in Figure 1.1. It consists of an X-ray tube (source) and a flat panel X-ray detector, both attached to a gantry that allows the coordinated rotation.

X-rays have the ability to penetrate biological tissue, to an extent that makes

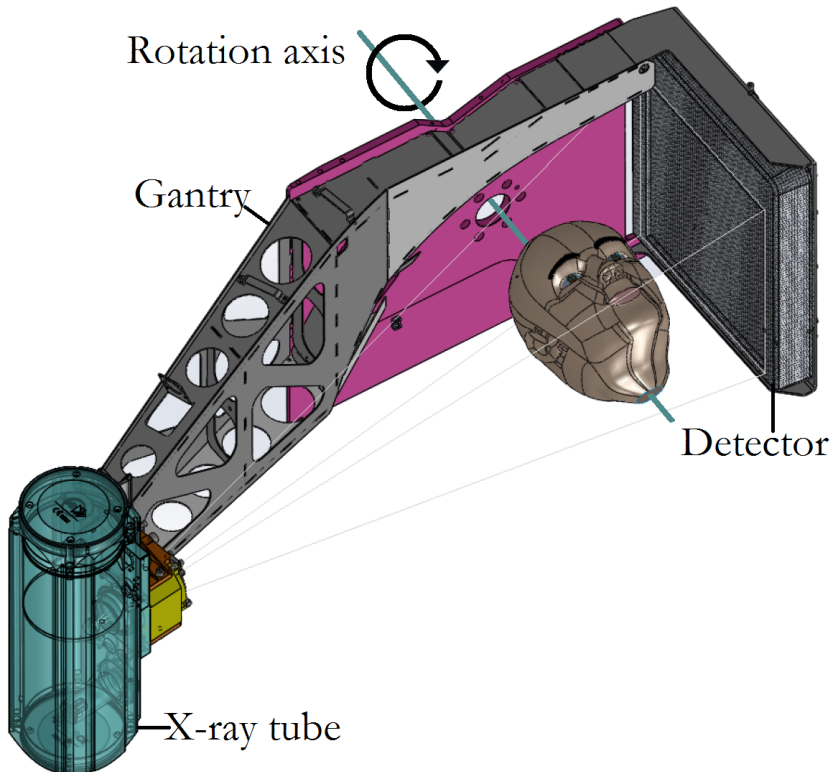


Figure 1.1: An illustration of the CBCT scanner and its relevant parts. The system rotates around the indicated rotation axis. Published with permission from Elekta AB.

them suitable for medical imaging purposes. Through a variety of interactions, some of the X-rays are absorbed or scattered on their way through the patient. The intensity of X-rays, finally reaching the detector, provides information about the extent of these interactions, and hence, about the patient.

1.1.1 CBCT in Radiosurgery

Elekta is currently working on a complete CBCT solution, that will be used in order to facilitate convenient and accurate patient positioning, in the context of non-invasive radiosurgery. A CBCT scanner will be attached to the new model of the Leksell Gamma Knife (Figure 1.2), which is used in hospitals around the world for treating brain lesions. In the future, the technology may also be used in additional applications.

1.1.2 Artifacts

CBCT imaging suffers from a number of artifacts, which causes the images to lose contrast. One important effect is the scattering of X-rays inside the patient, i.e., the

1.2. IMAGE CORRECTION



Figure 1.2: The new model of the Leksell Gamma Knife, named Perfexion Plus. The CBCT scanner can be seen in parked upright position in the center of the image. Published with permission from Elekta AB.

deviation from the otherwise straight trajectories. When incident on the detector, the scattered X-rays will act as noise, decreasing the contrast.

Another commonly characterized effect is called *beam hardening*. This has to do with the energy-dependence of the interactions between X-rays and matter. As an effect of this, the X-ray energy spectrum, i.e., the relative distribution of X-ray energies, will gradually shift as a beam from the source goes through the patient. Since higher X-rays of higher energy generally penetrate the tissue easier, the shift will be towards higher energies.

Other artifacts can be directly related to the response of the X-ray detector. This includes a smearing of the signal across adjacent pixels, limiting the spatial resolution. It has also been observed how residual signals, from previous images, are carried over into subsequent projections. This effect is sometimes referred to as *image lag* or *ghosting*.

1.2 Image Correction

In an effort to reduce the artifacts and improve the quality of the CBCT, Elekta has investigated several possible image correction applications. Such applications can either be used on the raw images, prior to the 3D reconstruction, or afterwards, in order to directly improve the final result.

An example of the latter is a Monte Carlo based method, simulating the transport of X-ray photons, through a reconstructed volume from a CBCT scan [1]. By observing how the result of the simulation differs from the originally reconstructed volume, the appropriate corrections can be made.

If properly characterized, some of the artifacts, related to the detector, can be removed directly from the raw images, prior to the reconstruction.

1.3 Problem Specification

For the image correction applications to be successful, a model of the X-ray detector response is necessary. The objective of this thesis is to develop a detector response model, which takes into account the smearing of the detected X-rays over adjacent pixels, as well as the time dependency of the response, causing a residue image in subsequent projection. This can be expressed in terms of a response function

$$R(\mathbf{r}, \theta, E, t), \quad (1.1)$$

where \mathbf{r} is the position and θ is the angle of an incident X-ray photon, E is its energy and t is the time.

Since much work has been done on characterizing flat panel detectors, a considerable part of the task will be to read up on current research, in order to establish what can be useful in this context. Another part will be to design experiments, which can be used to fit the developed models to the specific investigated detector.

1.4 Layout of thesis

A chapter, providing the necessary background theory, will follow directly after the introduction. This will enable a detailed description of the detector, given in Chapter 3.

After that, details concerning the spatial and temporal response of the detector are presented in two separate chapters. This is where the different parts of the response model are developed.

Chapter 6 describes the experimental methods used to verify the theoretical models and the results of the experiments are presented in Chapter 7. A deeper discussion is presented in Chapter 8, concerning physical interpretations, assumptions and error sources.

Finally, a brief summary of the thesis is given in Chapter 9.

2 | Background

Before addressing the specifics of the problem at hand, some general background theory is needed. This will concern mainly the properties of X-rays, their interaction with matter and the physical mechanisms that can lead to their detection. Some general properties of X-ray detectors and the materials used, will also be presented. The purpose of this is to paint a more general picture and to facilitate the detailed description of the studied detector, provided in Chapter 3.

Finally, an introduction to simulations of photon transport is given. This can be a very useful tool, when dealing with X-rays and their interaction with matter.

2.1 Electromagnetic Radiation and X-Rays

2.1.1 Definitions

Electromagnetic radiation is, as a consequence of its double nature, typically characterized by any of three physical properties. The frequency ν and the wavelength λ are due to the interpretation of electromagnetic radiation as a wave, whereas the photon energy E characterizes its particle nature. These two concepts are linked together by the Planck relation

$$E = h\nu, \quad (2.1)$$

where the photon energy is shown to be proportional to the frequency. The coefficient of proportionality is the Planck constant, $h = 6.626\ldots \cdot 10^{-34}$ Js. This can also be expressed in terms of the wavelength (in vacuum), using the relation

$$\lambda = \frac{c}{\nu}, \quad (2.2)$$

where $c = 2.998\ldots \cdot 10^8$ m/s is the speed of light.

X-radiation, or X-rays, is found in the higher energy part of the electromagnetic spectrum. It is commonly distinguished from the even higher energy gamma (γ) radiation by the nature of its origin. By this definition, γ -rays originate from the atomic nucleus, while the X-rays originate from the energy levels of the atom. In diagnostic medical X-ray imaging, the photon energy typically ranges from about 10 to 150 keV. This corresponds to a frequency of about $2 \cdot 10^{18}$ to $4 \cdot 10^{19}$ Hz and a vacuum wavelength of 0.1 to 10 nm.

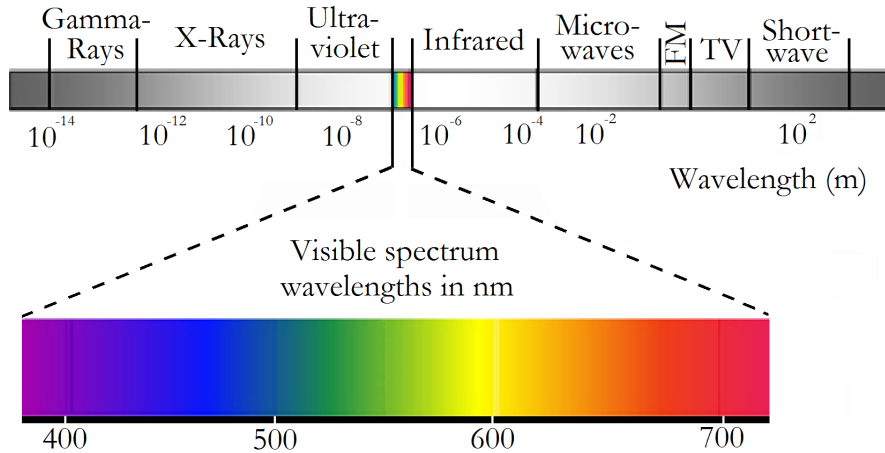


Figure 2.1: The electromagnetic spectrum.

The visible portion of the electromagnetic spectrum ranges from wavelengths of approximately 390 to 700 nm. Photons in the visible spectrum are often referred to as *optical photons*.

Note that the X-ray energies are given in electron volts (eV), or kilo electron volts (keV), where 1 eV corresponds to about $1.602 \cdot 10^{-19}$ J. This will be the convention throughout this thesis. Optical photons, on the other hand, are more commonly characterized by their vacuum wavelength.

2.1.2 X-ray Production

There are several different methods available to produce X-rays. The most common, and perhaps the simplest of these, is the method used in the standard X-ray tube. Free electrons are accelerated toward a positively charged anode, consisting of an adequately selected metal, such as tungsten (W). This results in the emission of photons in the form of *bremsstrahlung* and *characteristic X-rays*. Both are illustrated in Figure 2.2.

Bremsstrahlung

The word bremsstrahlung comes from the German language and is directly translatable to "braking radiation". It is well-known that a charged particle, when accelerated (or decelerated), emits electromagnetic radiation. This is exactly what happens to some of the electrons in the X-ray tube, when incident on the metal anode. Coulomb interaction with the heavy nucleus causes the electrons to bend off, resulting in the emission of photons. The radiated spectrum will be continuous, because of the continuous nature of the Coulomb interaction.

2.1. ELECTROMAGNETIC RADIATION AND X-RAYS

Characteristic X-rays

Radiation of characteristic X-rays occurs when the incident electrons interact with the electrons in the metal anode. The bound electrons are ejected from their specific quantized energy state, leaving behind a vacancy. These vacancies are subsequently filled by outer electrons of the atom. The step from a higher to a lower energy state, by an outer electron, results in the emission of a photon of characteristic energy. Since there are a number of different atomic levels, there are many possible transitions between these and hence many possible photon energies. These are nevertheless discrete, as opposed to bremsstrahlung.

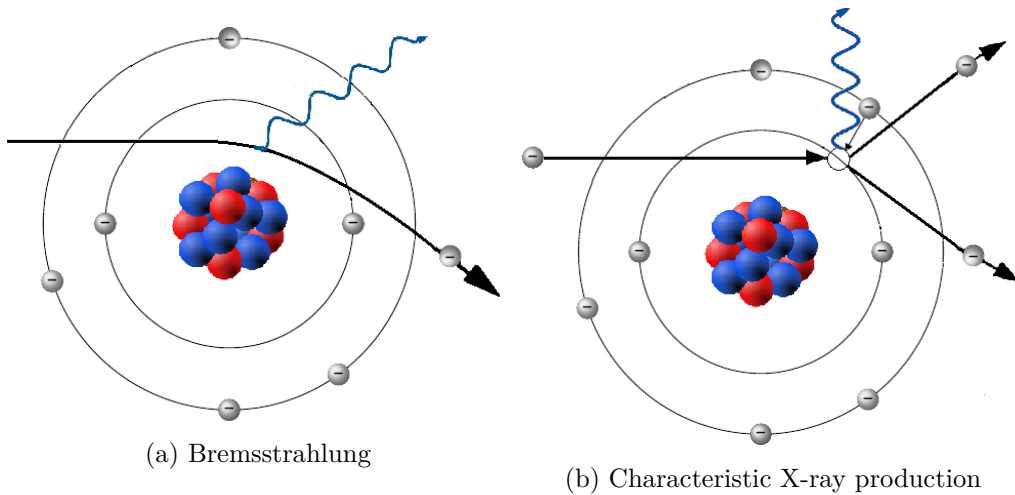


Figure 2.2: An illustration of the processes that result in the generation of X-rays.

The X-ray Tube Spectrum

Figure 2.3 shows a detailed X-ray spectrum, produced by a tungsten-rhenium X-ray tube. Three important features of the curve can be worth mentioning at this point.

The unit commonly used to describe the energy of the X-ray spectrum is *peak kilovoltage* (kVp), referring to the voltage applied across the X-ray tube. This will set a limit on the energy of the accelerated electrons, and thus also on the energy of produced X-rays. The spectrum in Figure 2.3 is produced using 80 kV. Consequently, there are no X-rays of higher energy than 80 keV.

Secondly, there are several characteristic peaks in the spectrum, originating from the characteristic atomic energy levels of tungsten and rhenium. This concerns primarily the K_{α} and K_{β} transitions, i.e., the transitions from the L-shell to the K-shell and from the M-shell to the K-shell, according to the classical atomic model by Bohr.

Finally, photon energies from 0 to 10 keV are almost completely absent in the spectrum. This is because they are self-attenuated in the metal anode, i.e., they are absorbed before they reach the surface. This will also limit the number of peaks

from characteristic transitions, present in the spectrum. Transition between higher orbitals of the atoms will have lower energies and will therefore not show up in the spectrum.

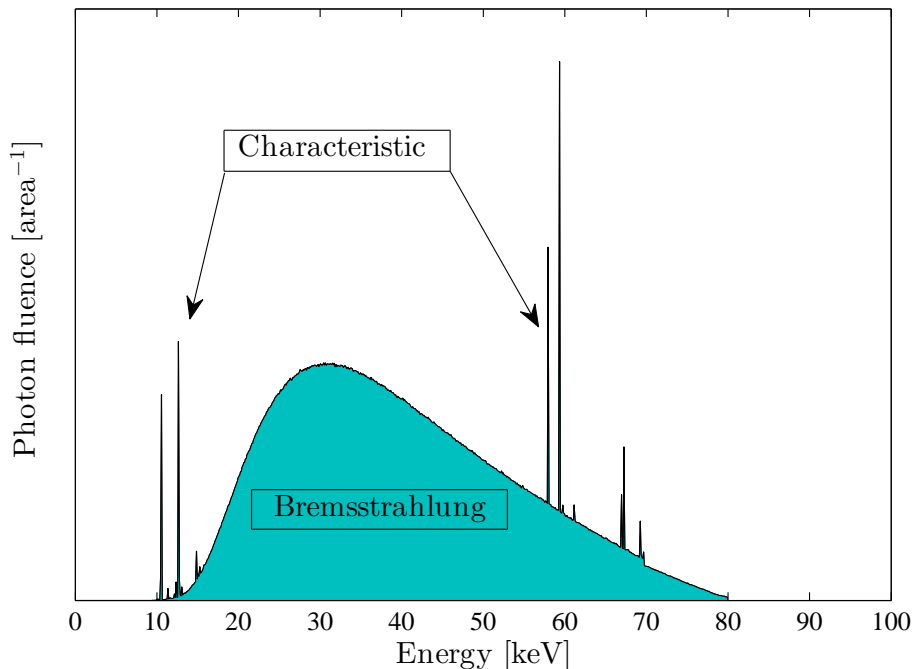


Figure 2.3: The spectrum from a tungsten-rhenium X-ray tube. Several characteristic X-ray energies are clearly visible, as well as the maximum energy at 80 keV.

2.2 X-ray Matter Interaction

The detection of X-rays can differ substantially, depending on detector type. They can include many different types of interaction and several steps, before an output signal is finally produced. In order to understand the principles of their operation, knowledge of the possible interactions between X-rays and matter is required.

2.2.1 Interaction Processes

There are several ways for the X-ray photons to interact with matter. The interactions may result in a local deposition of energy, which can be used to detect the X-rays. In some cases, the interactions also result in scattering, i.e., a deviation from the original trajectory of the photon. This may sometimes cause problems in medical imaging, as mentioned briefly in Chapter 1.

The important types of interaction between X-rays and matter are *the photoelectric effect*, *Rayleigh* (coherent) scattering, *Compton* (incoherent) scattering and

2.2. X-RAY MATTER INTERACTION

pair production. The underlying mechanisms and physical consequences of each interaction are reviewed here. All interaction are also illustrated in Figure 2.4.

The Photoelectric Effect

The discovery of the photoelectric in 1905 was one of the main contributions that gave Albert Einstein the Nobel Prize in physics, in 1921. The discovery also contributed greatly to the development of quantum mechanics and the concept of wave-particle duality of light.

The photoelectric effect is the complete absorption of an incident X-ray photon, by an atomic electron. After absorption of a photon of energy E_0 , the electron will get a kinetic energy, T , according to

$$T = E_0 - U, \quad (2.3)$$

where U is the binding energy of the electron.

Rayleigh (Coherent) Scattering

Coherent, or Rayleigh, scattering is the interaction with the electric field of an atom, resulting in the elastic scattering of the incident photon. Elastic means that no energy is transferred to the electron and the result is simply a deviation from the otherwise straight X-ray trajectory.

Compton (Incoherent) Scattering

The incoherent, or Compton, scattering is something in between photoelectric effect and Rayleigh scattering, in the sense that energy is partially transferred from the photon to the atomic electron. This type of interaction often occurs when the photon energy greatly exceeds the electron binding energy. The result is both a scattered photon, with decreased energy, and a free electron.

By considering the conservation of momentum and energy, the following expression can be derived for the energy of the scattered photon

$$E' = \frac{E_0}{1 + \frac{E_0}{m_e c^2} (1 - \cos \phi)}, \quad (2.4)$$

where E_0 is the energy of an incoming photon, m_e is the electron mass and ϕ is the scattering angle. In the derivation of eq. 2.4, it is assumed that the binding energy, U , is equal to 0. With this approximation, the kinetic energy of the electron simply becomes

$$T = E_0 - E'. \quad (2.5)$$

Pair Production

Pair production differs from the previously described interactions in that it is not an interaction between photon and electron, but between photon and atomic nucleus. In this interaction an electron-positron pair is created, utilizing the energy of the incident photon. Considering the conservation of momentum and energy, it is not difficult to show that this requires a photon energy greater than 1.02 MeV. Note that this is much greater than the energies normally used in diagnostic X-ray imaging.

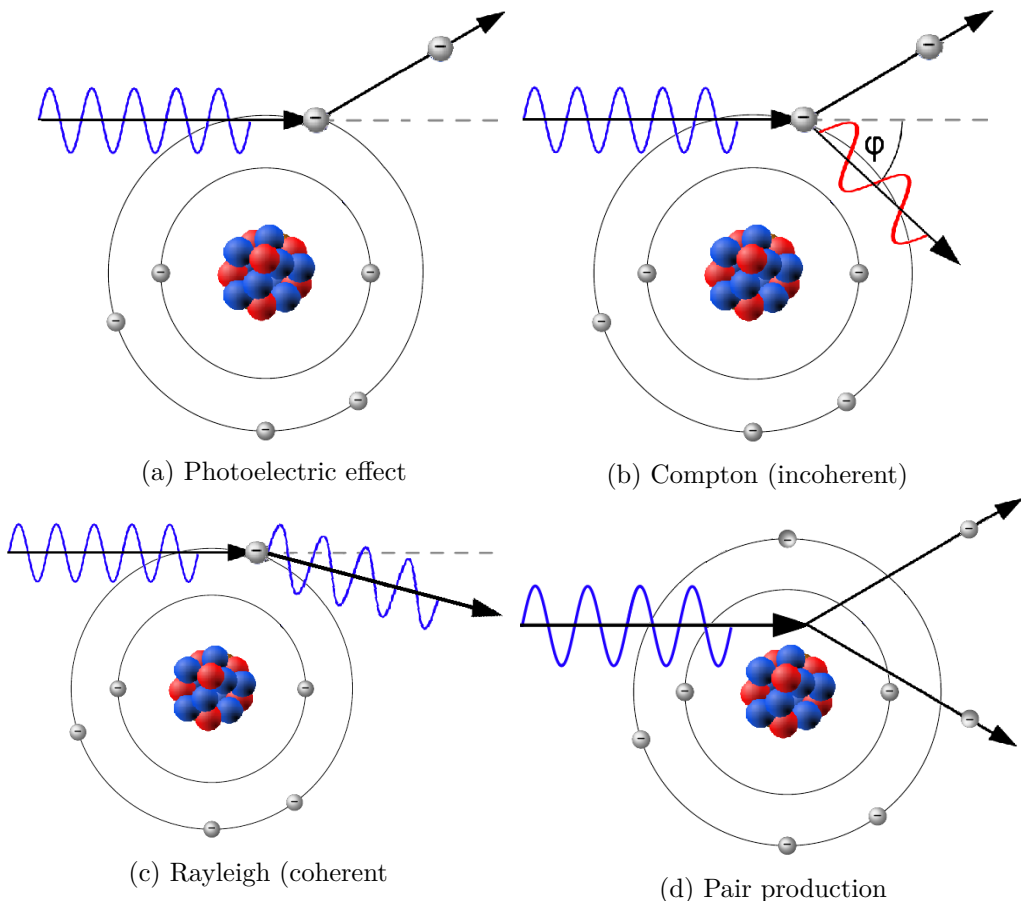


Figure 2.4: An illustration of the most important X-ray matter interactions.

2.2.2 Attenuation

As a beam of X-rays enter a material, photons are gradually lost due to scattering or absorption events, according to the interactions, discussed above. This effect is called *attenuation*.

Consider a thin beam of N photons, incident on a piece of matter of thickness dx . Denoting the probability of interaction μdx , the change in the number of photons

2.3. ELECTRONIC BAND STRUCTURE

can be written

$$dN = -N\mu dx. \quad (2.6)$$

This can be integrated to obtain an expression for the gradually decreasing number of photons, as the beam moves through a material of arbitrary thickness,

$$N = N_0 e^{-\mu x}. \quad (2.7)$$

μ is called the linear attenuation coefficient. This is a sum of attenuation due to all different interactions causing scattering or absorption of X-rays,

$$\mu_{tot} = \mu_{PE} + \mu_{Com} + \mu_{Ray} + \mu_{pair}. \quad (2.8)$$

The different attenuation coefficients not only depend on material parameters, but also on photon energy. Both dependences are important to take into consideration, when designing X-ray detecting equipment.

Beam Hardening

As described in the previous section, the X-ray tube produces a spectrum of energies, ranging up to its specific kVp. The dependence of the attenuation on the photon energy will hence cause a non-uniform decrease in photon number over the beam spectrum. The higher-energy photons normally penetrate the material easier, which results in an energy spectrum that gradually shifts toward higher energies. This is the, so called, *beam hardening* effect, which was briefly mentioned in Chapter 1.

2.3 Electronic Band Structure

When considering the electron in a solid, the Bohr model is generally not sufficient. In a crystalline material, the electrons are not only bound in their respective atoms, but rather shared over the periodic lattice of atomic nuclei. The possible energy states of the electrons can be found by solving the Schrödinger equation, asserting periodic, so called, Bloch functions.

The solutions to the Schrödinger equation form an energy band structure. The bands describe allowed and forbidden energy intervals of the electrons, and their structure determines many important physical properties of the solid.

The highest energy band that is occupied at absolute zero temperature, is called the *valence band*, and the lowest unoccupied band, at zero temperature, is called the *conduction band*. The energy difference between these two is an important material parameter, called the *band gap*, E_g . The discrete transition between these two bands can lead to both emission and absorption of specific types of radiation.

Semiconductors have a band gap of around 1 eV, meaning that electrons from the valence band are easily excited to the conduction band, by thermal energy or optical photons. Insulators are materials of higher band gap, requiring higher

energy to excite the valence electrons. Metals, on the other hand, already have some electrons located in the conduction band, resulting in a high electric conductivity. The materials, examined in this thesis, will mainly be of the semiconducting or insulating type.

The principles of energy band structure in the three types of materials are illustrated in Figure 2.5. It also shows the *Fermi level*, which is used to describe the surface of the electrons energies at absolute zero temperature.

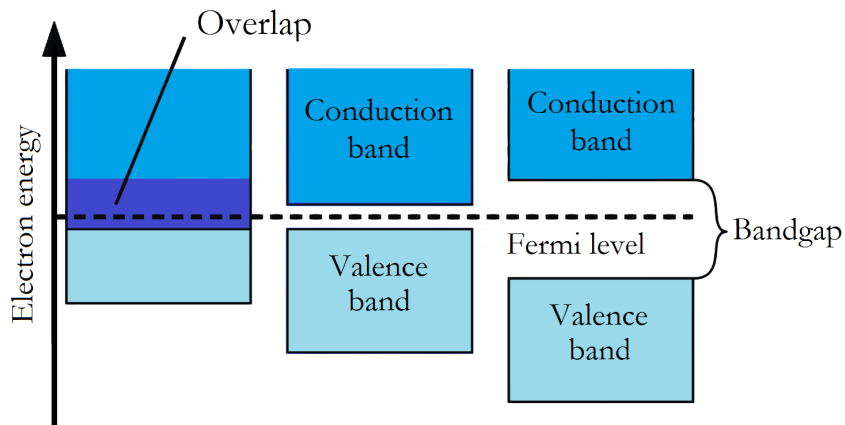


Figure 2.5: The principles of energy bands in metals, semiconductors and insulators.

2.3.1 Doping

The intentional incorporation of a small fraction of impurities in the original material can modulate the electronic band structure and thus change its electronic properties. This is the concept of *doping*. The impurities are in the form of atoms with a different number of valence electrons than the original material. This will result in either an extra electron (n-doping), or a so called hole (p-doping), in the otherwise forbidden band gap. A hole is simply the absence of an electron, conveniently described as a pseudo-particle.

The change in electronic band structure, as a result of n- and p-doping, is shown in Figure 2.6. The n-doping will effectively raise the Fermi level, thus decreasing the energy needed to excite electrons into the conduction band. p-doping will introduce holes in the band gap, hence facilitate the excitation of electrons from the valence band. In both cases, the band gap will be decreased.

2.3.2 Conductivity and Charge Trapping

As the name suggests, electrical conduction is normally carried out by electrons in the conduction band. If there are holes present in the valence band, also they contribute to the current. Since holes have positive charge, they travel in the opposite direction, compared to the electrons.

2.4. DIGITAL X-RAY DETECTORS

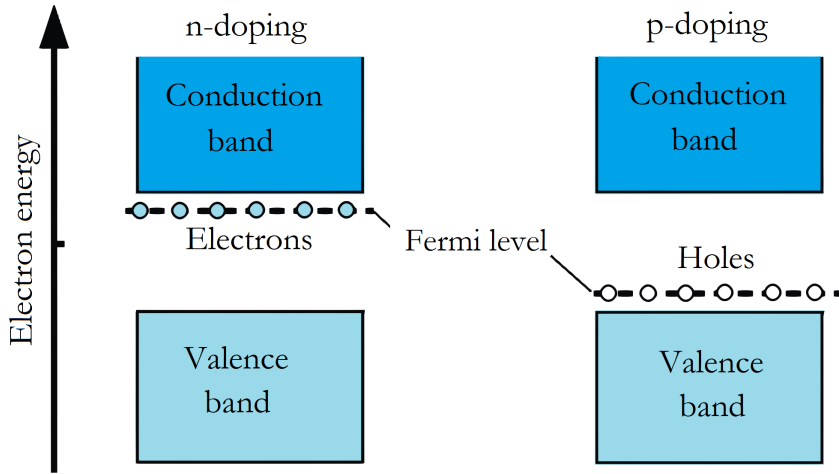


Figure 2.6: The principles of n- and p-doping.

In disordered or partially disordered (amorphous) materials, the atoms are not positioned with complete periodicity. This leads to modifications of the electronic band structure. Irregularities in the material result in many dangling inter-atomic bonds, which create new possible energy states in the, otherwise forbidden, band gap. An allowed state in the band gap often referred to as a *localized state*. The irregularities will also lead to a smearing of the band structure, resulting in tails of allowed states, extending far into the forbidden regions [24].

Depending on where in the band gap it is positioned, the state is more or less stable (metastable). A free charge from the conduction band can thus fall into the available state and stay there for some time, that will depend on the energy of the state. This is the concept of *charge trapping*. Charge carriers in a metastable, localized state will here be referred to as *trapped charge*.

Charge trapping influences the electronic properties of a material and can lead to noticeable phenomena in many different electrical components [24]. This is treated later in this thesis, when the temporal characteristics of the detector response are investigated.

2.4 Digital X-ray Detectors

With the provided theory of X-rays, their interaction with matter and energy band structure of solids, it is possible to explain the principles of digital X-ray detectors. The dominating technology for this application is the flat panel active matrix array, which is also used in computer screens as well as many other types of displays. Detectors utilizing this technology are commonly referred to as flat panel detectors.

Two general types of flat panel detectors are typically distinguished, *direct* and *indirect*.

2.4.1 Direct Detectors

In direct detectors, the incident X-rays are directly converted into charge carriers in a photoconducting material, like silicon (Si) or selenium (Se). The charge carriers produce an output current in the specific pixel, in which the X-ray was absorbed. This current is (ideally) proportional to the intensity of the incident radiation.

2.4.2 Indirect Detectors

Indirect detectors also utilize a photoconducting material, that converts photons into an output current. The difference from direct detectors lies in the nature of the initial X-ray detection. Indirect detectors incorporate a scintillating material, which converts the incident X-rays into lower-energy optical photons. These are then detected, as they reach the base of the scintillating layer.

Although the indirect approach is efficient in the conversion of X-rays into a measurable output signal, some complicating effects normally occur. These effects include a spatial spread of the optical photons, created in the scintillating layer, across adjacent pixels.

A more detailed description of indirect detectors in general, and the examined detector in particular, will be given in Chapter 3.

2.5 Monte Carlo Methods

Monte Carlo computational algorithms is a broad class of methods that use chance, or randomness, to obtain their results. The basic idea is to produce a sufficiently large number of events, all at some point influenced by the element of chance. The results can then be evaluated, e.g. by picking out the most successful solution or by computing averages over obtained distributions.

In photon or particle tracking, individual particles are followed through a material and interactions, such as absorption or scattering, occur stochastically, according to certain pre-decided probabilities. Meanwhile, data of interest is collected, stored and accumulated. The distributions obtained through the simulations can provide very detailed information about the behaviour of radiation in the material. The important advantage that no simplified assumptions have to be made in order to make possible an analytical solution. Monte Carlo methods can therefore be a powerful tool in the study of X-rays and X-ray detectors.

3 | Flat Panel Scintillator X-ray Detector

The detector, studied in this thesis, belongs to the category of indirect flat panel detectors. The indirect property refers to the incorporation of a scintillator material, that converts the incident X-rays into visible, or optical, photons. These are then detected as they reach the base of the scintillator, which is attached to a large area integrated circuit, called the *active matrix array* (see Figure 3.1).

In a bit more detail, the detector consists firstly of a thallium doped caesium iodide (CsI:Tl) scintillator, structured in the shape of thin crystal columns. The columns are supposed to work similarly to optical fiber cables, preventing a too large spatial spread of the signal. The detection of the optical photons is implemented through a matrix of amorphous silicon (a-Si) photodiodes, preferably taking up the larger part of the active matrix array area. Each photodiode, together with TFT switching device and charge pre-amplifier, constitutes what is commonly known as a pixel.

This chapter aims at describing in detail the function of the flat panel scintillator detector. This will clarify what is needed of an adequate response model.

3.1 Scintillator

The definition of a scintillator very much resembles that of a phosphor, which is also a material that re-emits the energy from an incoming particle, in the form of light. The nuance between the two is related to the speed of which this re-emission occurs. Scintillation refers to the fast emission of light, which is an important feature in the context X-ray detection.

The material used for this purpose is caesium iodide (CsI), doped with thallium (Tl) impurities. A detailed description of the material and its properties is given below.

3.1.1 Attenuation

CsI has the ability to attenuate the incoming X-rays in a relatively short distance. This is done almost exclusively through the photoelectric effect, as long as the

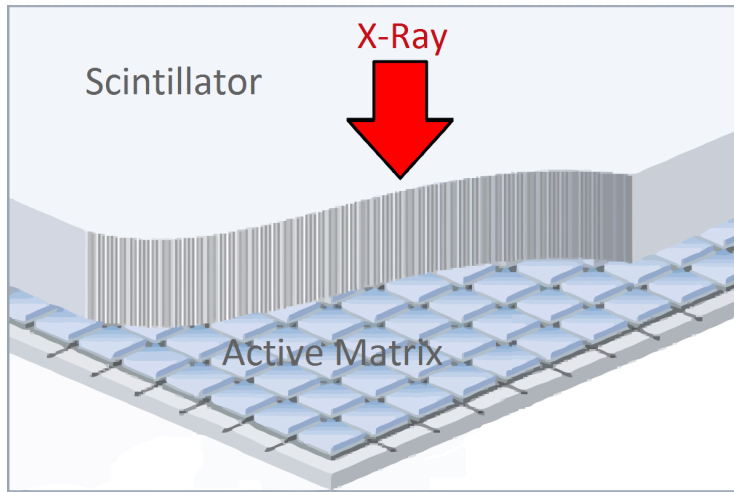


Figure 3.1: A cross section of the flat panel scintillator detector.

energies stay below a few hundred keV.

In Figure 3.2, the attenuation of CsI is plotted as a function of the photon energy. The numbers can be found in *XCOM: Photon Cross Sections Database*, provided by the National Institute of Standards (NIST) [29]. The total attenuation, the photoelectric effect, coherent scattering and incoherent scattering are all included in the plot. Note that the attenuation is given in the unit cm^2/g (*mass attenuation coefficient*). This value has to be multiplied by the density, in order to give the attenuation per length (*linear attenuation coefficient*). The density of CsI is 4.51 g/cm^3 .

3.1.2 Energy Band Transitions and Optical Spectrum

A general review of electronic band structures in solids was given in chapter 2. The characteristics like the energy gap, E_g , were described as important features of a material.

It is the de-excitation of electrons, from the conduction band to the valence band, that causes the emission of light in scintillators. To obtain the right photon energy, the band gap has to be adjusted accordingly. CsI is an insulating material, with a band gap at around 6.4 eV [25], which would give photons in the ultraviolet (UV) range.

Some scintillators have incorporated impurities, called activators, which modify the band gap structure in order to obtain specific de-excitation energies. This is exactly the role of the Thallium (Tl) in CsI:Tl. Figure 3.3 shows a typical band structure of a scintillator material with an activator. At the sites of the Tl impurities, the band gap will be lowered, resulting in energy transitions of around 2.5 eV. This corresponds to wavelengths of around 500 nm, which is well within the optical spectrum.

3.1. SCINTILLATOR

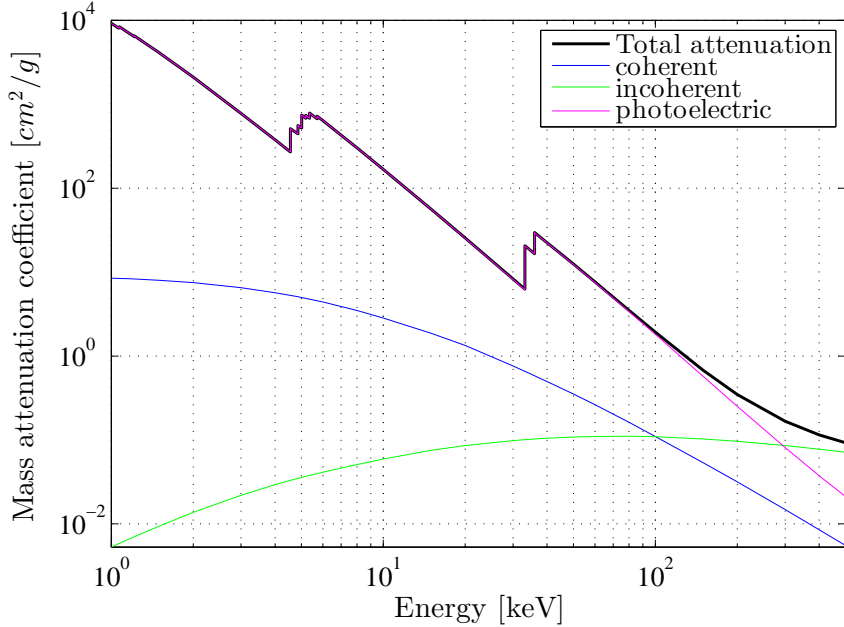


Figure 3.2: X-ray attenuation in CsI. The plot includes all present interactions for energies of 1-150 keV [29].

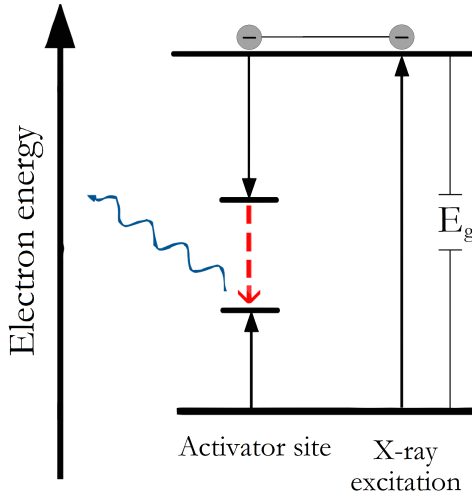


Figure 3.3: Energy band diagram for the activated scintillator.

The detailed spectrum of optical photons from the scintillator is generally of interest. It will be of importance when designing the sensing element of the active matrix array, which should be highly sensitive for these particular wavelengths. Many experimental measurements of emission spectra of CsI:Tl have been performed, e.g. by Valentin et al. [27] and Gwin and Murray [9]. They are also usually given by the

producers of scintillating crystals, in their technical specifications. Such emission spectra is shown in Figure 3.4, for Tl doped and sodium (Na) doped CsI.

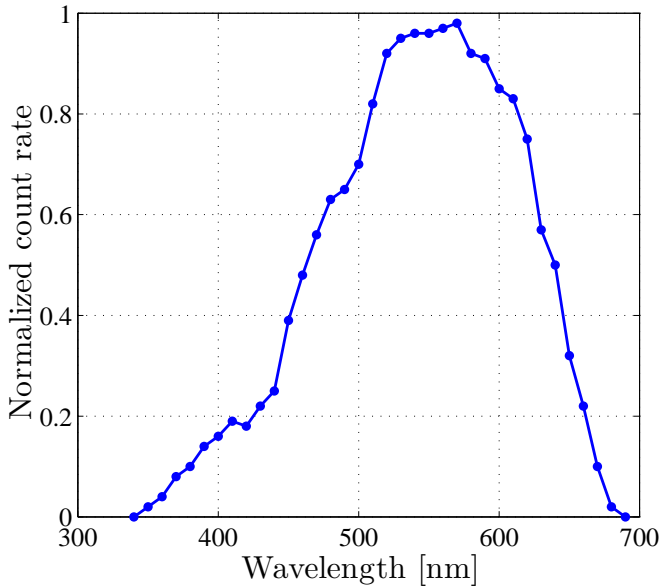


Figure 3.4: The emission spectrum of a CsI:Tl scintillator, as measured by Valentin et al. [27].

3.1.3 Decay Times

As mentioned in the beginning of this section, the time frame in which light emission occurs, is an important property of the scintillator. This is described by the decay time, τ , defined as the time between excitation and de-excitation, i.e., emission of an optical photon.

CsI:Tl has been shown to have two characteristic decay times, one fast and one slow [27]. The fast one is $0.68 \mu\text{s}$ and the slower is $3.34 \mu\text{s}$. They are responsible for 64 % and 36 % of the produced light, respectively.

A quick estimate of the measurement time shows that the scintillator decay time is so small, that it can be considered instantaneous. The examined CBCT scanner normally takes 10 images per second, giving a time between each image of 100 ms. This is in the order of 10^5 times the decay time. Even if using a significantly higher rate, the decay time can be taken to be zero.

3.1.4 Conversion Gain

The energy from the incident X-rays photons is what causes the excitation of the scintillator, which is followed by de-excitation and the emission of optical photons. However, the excitation process is not as simple as that, and not all incoming X-

3.1. SCINTILLATOR

ray energy is converted into optical photons. Out of the interactions, described in chapter 2, the photoelectric effect is the most prominent in the scintillator (see Figure 3.2). This process results in both secondary X-rays and free electrons, which continue to interact with the material.

The number of optical photons created by an absorbed X-ray is called the *scintillation yield*, most commonly given in units of counts per keV X-ray. This number has been carefully measured to be 65 keV^{-1} for CsI:Tl [27]. Still, values given in literature [5] [11] and by manufacturers can differ by as much as 10 keV^{-1} .

K-Fluorescence Escape

The scintillation yield is very close to linear in X-ray energy [11], i.e., the number of optical photons per keV X-ray is constant. Over certain energies, however, the number of optical detected photons starts to deviate from this linear relation. This is due to an effect called *k-fluorescence escape*, which means that certain secondary X-rays escape from the material without contributing to the production of optical photons.

This effect occurs when X-ray energies exceeds the minimum energy required to excite electrons in the K-shell to the L-shell in Cs (35.985 keV [4]) and I (33.169 keV [4]). In the de-excitation of these electrons, secondary X-rays are emitted, which have the ability to escape without detection. As mentioned in chapter 2, this particular transition is called the K_{α} -transition. Similarly, the transition between the M-shell and the K-shell is called the K_{β} transition.

3.1.5 Optical transport

The conversion gain, i.e., the strength of the output signal depends on the thickness of the scintillator. The thicker material, the higher probability of interaction with the X-rays and more energy is converted into light. However, the physical structure of the scintillator has a significant effect on the spatial spread, or blurring, of the response.

Figure 3.5 illustrates how different designs of the scintillator layer influence the response of optical photons. The possible designs include different thicknesses, adding a reflective or absorptive layer as well as modifying the crystal structure of the material. Generally, an increased conversion gain comes to the cost of a larger spatial spread.

The most successful design is the column structured CsI, which decreases the blurring, without significantly decreasing the conversion gain. The columns work as fiber-optic light guides, as a consequence of the difference in refractive index of the CsI ($n_{CsI} = 1.80$) and surrounding gas ($n_{gas} \approx 1$).

To increase the absolute light output, a thin reflective coating, e.g. aluminium, can be applied to the top of the scintillator. This layer will be easily penetrated by the X-rays, while optical photons will be almost completely reflected and directed

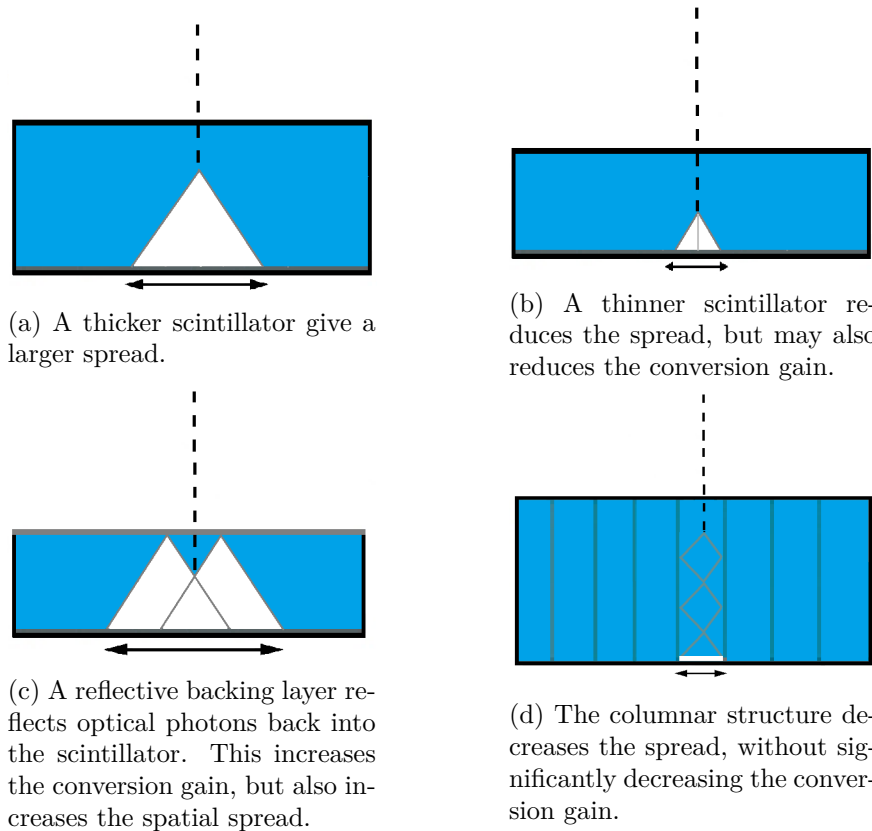


Figure 3.5: Different possible designs of the scintillating layer result in different spatial spread of the optical photons.

back into the scintillator. Note that this method to increase the light output will also increase the spatial spread of the signal.

The detector, specifically studied in this thesis, has a scintillator consisting of columnar CsI:Tl. However, not much more is known about the detailed structure. The provided technical specifications are not very detailed on the subject, and the manufacturer of the detector maintains a restrictive attitude towards releasing any kind of technical data.

3.2 Active Matrix Array

The detection and registration of optical photons from the scintillator is carried out by the active matrix array. Similarly to a modern computer or television screens, it consists of a large number of pixels, which are actively controlled by peripheral circuitry through a matrix of conducting lines.

The design of the active matrix array, and in particular the individual pixel, is described below.

3.2. ACTIVE MATRIX ARRAY

3.2.1 Sensing Element

The sensing element of the active matrix array is typically a photodiode, a semiconductor component, sensitive to light in the visible spectrum. This is what finally detects the optical photons from the scintillator and converts them into an electrical signal.

The charge created through photo-excitation will be stored on the sides of the photodiode, which thus acts as a capacitor. The intrinsic capacitance can be described by the simple parallel-plate formula

$$C_{pd} = \epsilon_r \epsilon_0 A / d, \quad (3.1)$$

where ϵ_r is the dielectric constant of the semiconductor, ϵ_0 is the vacuum permittivity, A is the area and d the thickness of the photodiode.

The studied detector has a pixel size of 0.184 mm×0.184 mm, however, it is usually run in a mode where squares of four pixels are combined and seen as one. The effective pixel size is therefore 0.368 mm×0.368 mm. The area of the individual photodiodes, A , is of the same order, but slightly smaller in order to make room for the circuitry.

A more thorough discussion about the physics of the photodiode is given in a separate section, following this general discussion of the active matrix array.

3.2.2 TFT Switching Device

In order to register the signal from the pixel, the charge has to be actively transferred from the photodiode to the peripheral circuitry of the active matrix array. A thin film transistor (TFT) is used to achieve a fast switching between the the read-out state, called the *on state*, and the *off state*. The switching is controlled by a gate voltage, V_g , applied over the specific row of the active matrix array, where the pixel is located.

The TFT has been studied and used extensively, e.g. in LCD screens, and a detailed physical description will not be given here.

3.2.3 Read-out Process

In Figure 3.6, a schematic circuit diagram is given for a single pixel in the active matrix array. In the beginning of a read-out cycle, the voltage at the connection point between the sensing element and the switching element, denoted V_A , is basically zero. When optical photons from the scintillator are incident on the photodiode, a signal current, I_{sign} , is created, which leads to charge being stored through the intrinsic capacitance, C_{pd} . This increases the value of V_A , which moves towards the applied voltage, V_{bias} .

During the read-out, the sensing element is connected to the peripheral circuitry by the gate voltage of the TFT. Because of the finite V_A , the charge from the

photodiode is transmitted to a charge pre-amplifier, finally resulting in an output voltage, V_{out} .

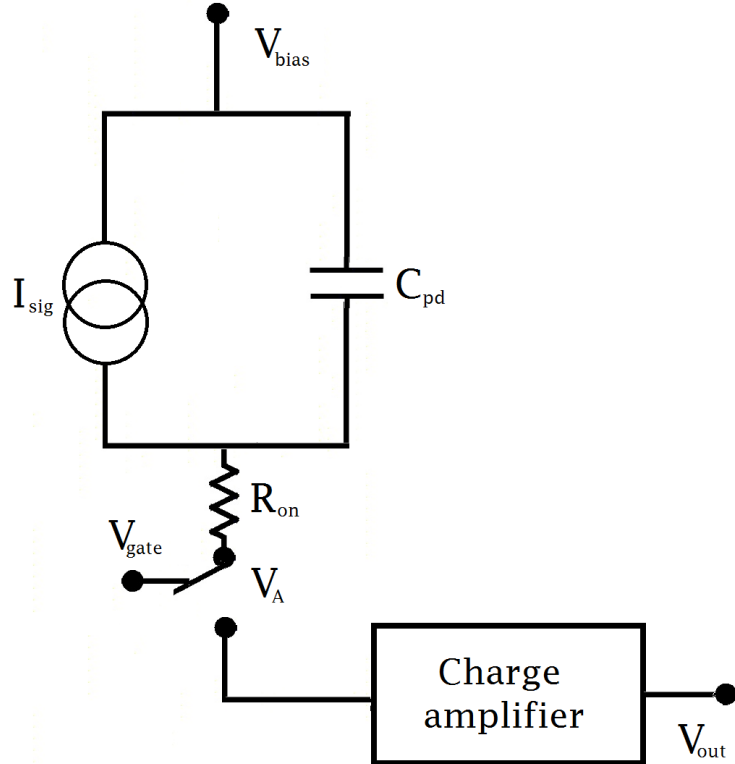


Figure 3.6: A simplified circuit diagram of a single pixel in the active matrix array.

3.2.4 The Fill Factor

The size of the pixel will of course influence the resolution of the detector. This is assuming that the blurring from the scintillator is not too significant. On the other hand, decreasing the size of the pixel may result in a smaller fraction of the pixel area being sensitive to incoming light, since a large part is taken up by the TFT and other circuitry. This fraction of the area, sensitive to incoming radiation, is an important property known as the geometrical fill factor.

3.3 Photodiode Sensing Element

The semiconducting material, used in the photodiodes of the studied detector, is hydrogenated amorphous silicon (a-Si:H). Amorphous means the non-crystalline form of silicon, which is less ordered than e.g. the polycrystalline or the crystalline form. Amorphous silicon has an absorption coefficient approximately one order of magnitude higher than the crystalline form, for photons in the visible range.

3.3. PHOTODIODE SENSING ELEMENT

A reader familiar with the concepts of quantum mechanics may note that this is due to the relaxed momentum selection rules, as a consequence of the intrinsically disordered nature of a-Si.

The reason for the hydrogenation is to passivate the many dangling intermolecular bonds in the amorphous structure, which affect the electrical and optical properties of the silicon [24].

An a-Si:H photodiode can be designed in a number of different ways. Regardless, the principles regarding detection of incoming light are the same. To understand the basic physics of the photodiode, we consider the simple cases of a *p-n junction* and the *p-i-n junction* (see Figure 3.7).

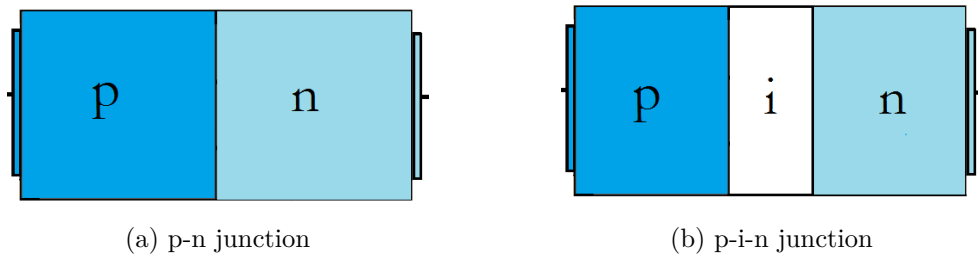


Figure 3.7: A simplified Figure to illustrate the structure of a p-n junction and a p-i-n junction.

3.3.1 The p-n Junction

Band Structure of a p-n Junction

Energy band structure in solids, and the concept of doping, was introduced in chapter 2. It was described how the incorporation of extra electrons (n-doping) or holes (p-doping) modifies the band structure of materials and change their electronic properties.

The junction of n- and p-doped semiconductor forms a simple type of diode, known as a p-n junction. As a result of the injected electrons and holes on the respective sides, the band structure of the junction will be changed according to Figure 3.8. Some of the electrons from the n-side will diffuse across the junction and recombine with holes on the other side. This creates a, so called, depleted region, preventing any further migration of electrons and holes.

Current-Voltage Characteristics

The current-voltage (IV) characteristics of the p-n junction, shown in Figure 3.9, makes it very useful in many electronic circuits. When applying a forward bias voltage to the junction, above some characteristic value, a current will start to flow with very low resistance. However, a reverse bias will not have the same effect.

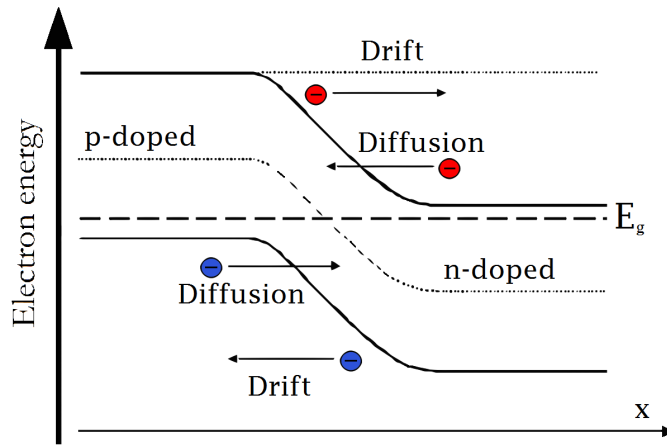


Figure 3.8: The energy band structure of a p-n junction.

This is because the depleted region will even out the potential of the holes and the electrons, resulting in no, or a very small, current.

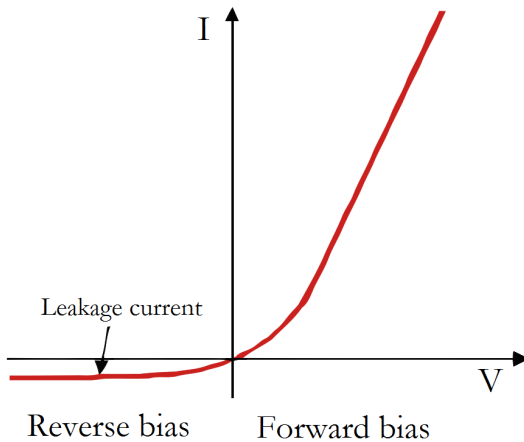


Figure 3.9: Current-voltage characteristics of the p-n junction.

Photo-excitation in the Band Structure

Optical photons of sufficient energy have the ability to excite electrons from the valence band, resulting in an electron-hole (e-h) pair. When this happens in, or close to, the depletion layer, the charge carriers will tend to diffuse over to their respective sides. However, without an applied voltage, the chance of recombination is impending, and the output current will be small. That is why a reverse voltage is applied to the junction, helping the charge carriers to get across the junction and increasing the efficiency of the photo-detection.

3.4. MODELLING THE DETECTOR RESPONSE

The applied reverse voltage will also result in a small leakage, or thermal, current, according to the IV characteristics in Figure 3.9. A balance therefore has to be found between the detection efficiency and signal noise, caused by this leakage.

3.3.2 The p-i-n Junction

In the sensing element of the active matrix array, it is necessary to have a high efficiency, in the conversion of optical photons into stored charge. This is often referred to as a high quantum efficiency. For that reason, the depletion layer, where the conversion takes place, should be made thick enough to absorb all incoming photons.

In a n-i-p junction, an intrinsic (undoped) layer is put between the doped layers. The depletion region will extend all the way across the intrinsic layer, thus enabling a high quantum efficiency.

3.4 Modelling the Detector Response

So far in this chapter, the detector and its important components have been described. This theory provides a basic idea about what is needed of an adequate response model.

A model of the detector can, at least in a first order approximation, be conveniently separated into two main parts. These are the spatial spread of the response, and the temporal delay, or broadening. The former is due to the creation and transport of optical photons through the scintillator material, before they reach the pixels of the active matrix array. The latter part may depend on several mechanisms, such as delayed decay of the scintillator, incomplete charge transfer from the photodiodes or charge trapping in the bulk a-Si:H. The two parts of the response model will be treated in separated chapters, following directly after this.

Note that the limited information about important parameters, such as the scintillator thickness, will make the modelling considerably more complicated. This means that the theoretical derivations have to be kept more general, leaving gaps that must be filled with information from experimental measurements.

4 | Point Spread Function

The objective in this chapter is to find the *point spread function* (PSF) of the columnar CsI:Tl scintillator. The PSF is the response (of optical photons) from a point source, which in this case means a thin beam of mono-energetic X-rays. For simplicity, the point of incidence is assumed to be $(x, y, z) = (0, 0, 0)$. This is nothing more than a translation and will not affect the generality of the discussion. As described in previous chapters, the dependence on incident angle, (θ, ϕ) , and the X-ray photon energy, E , will also be taken into account.

The coordinate system is shown in Figure 4.1. The angles θ and ϕ are the usual spherical angles, defined according to Figure 4.2.

4.1 An Analytical Model of the Scintillator Response

In a paper from 2010, Freed, Park and Badano [7] present an analytical model of the response of a CsI scintillator. The model is based on a few general physical assumptions, which would apply to almost any scintillator detector. The general model is then adopted to a certain detector type, by comparing with results from detailed Monte Carlo simulations [7] [3].

The simplicity and generality of the model by Freed, Park and Badano will be appropriate for the current investigations, since many details about the detector are

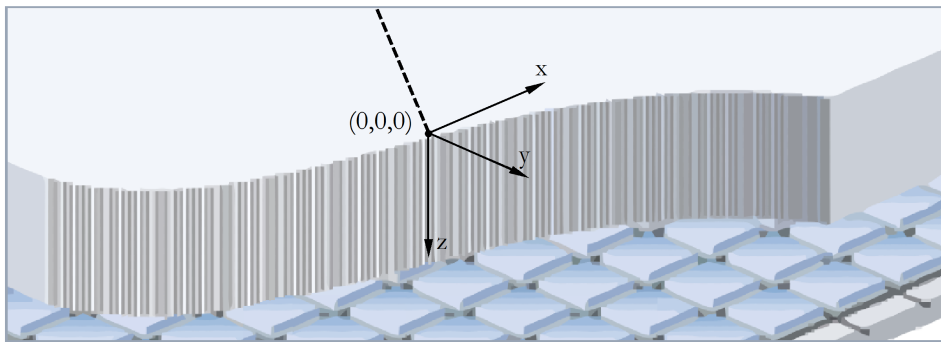
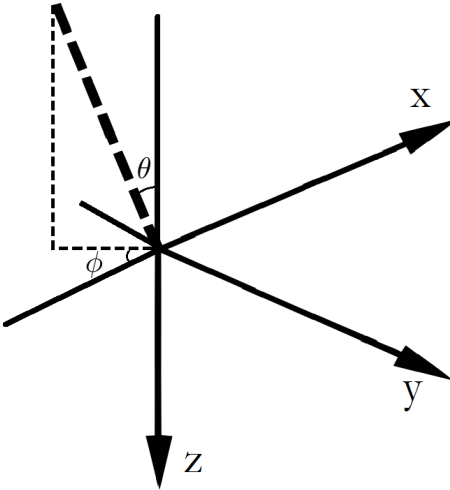


Figure 4.1: A thin X-ray beam (dashed line), incident on a cross section of the detector. The coordinate system shown in the figure will be used throughout the discussion on the PSF.

Figure 4.2: The definitions of the angles θ and ϕ .

unknown. After obtaining a general analytical result, experimental measurements can be used, instead of simulations, to find the missing parameters.

4.1.1 A Simplified Physical Model

The simplified physical model, by Freed, Park and Badano [7], consists of four main parts. These are

1. the depth-dependent absorption of incident X-rays,
2. the creation of optical photons in the CsI,
3. the absorption of optical photons in the CsI and the collection at the base,
4. the depth-dependent spatial spread of the optical photons.

This will give a response function, which, in addition to x, y, E, θ and ϕ , also depends on the absorption depth, z . This function will be denoted $PSF_z(x, y, z, \theta, \phi, E)$.

The next step will be to integrate this over z , in order to obtain the total PSF,

$$PSF(x, y, \theta, \phi, E) = \int_0^{z_{max}} PSF_z(x, y, z, \theta, \phi, E) dz. \quad (4.1)$$

If the integrand in eq. 4.1 is simple enough, it will be possible to evaluate the integral analytically. The rest of this section will describe the physical models, used in the derivation process.

Absorption of X-rays

The analysis will be restricted to the case, where optical photons are only produced through the photoelectric effect. This is a reasonable approximation, as discussed in chapter 3. A detailed plot of the attenuation coefficients was given in Figure 3.2.

4.1. AN ANALYTICAL MODEL OF THE SCINTILLATOR RESPONSE

The photoelectric effect constitutes 90-99 % of the total attenuation in CsI, for X-rays up to 100 keV.

Using the notation of [7], the probability of photoelectric interaction at a depth z , can be written as

$$\eta(z, \theta, \phi, E) = \mu_{PE}(E) \exp(-\mu_{tot}(E) \cdot l), \quad (4.2)$$

where $\mu_{tot}(E)$ and $\mu_{PE}(E)$ are the total and the photoelectric attenuation constants of CsI, and l is the distance travelled in the material. Rewriting l in terms of the depth, z , we get

$$\eta(z, \theta, \phi, E) = \mu_{PE}(E) \exp\left(-\frac{\mu_{tot}(E)z}{\cos \theta}\right). \quad (4.3)$$

Creation of Optical Photons

The X-rays produce a number of optical photons, given by the function $K(E)$. We write the average number of optical photons, produced by an absorbed X-ray photon at a depth, z , as

$$N_{opt}(z, \theta, \phi, E) = K(E)\eta(z, \theta, \phi, E). \quad (4.4)$$

According to Knoll [11], $K(E)$ can be written as a linear function of the X-ray energy

$$K(E) = \gamma E, \quad (4.5)$$

where the gain factor $\gamma \approx 65 \text{ keV}^{-1}$ for CsI:Tl. Since γ is nothing more than a multiplicative factor, it is redundant in this discussion. The next steps of the derivation will introduce unknown coefficients, which will later be determined through experiments. Hence, γ will be dropped at this point.

Note that this model does not take into account the possible effects of K-fluorescence escape. As discussed briefly in Section 3.1, this is the escape of secondary X-rays, produced in the scintillator. In order to account for this effect, the linear expression $K(E)$ would have to be replaced by a more detailed function.

Absorption of Optical Photons and Collection Efficiency

To account for the optical photons being scattered or absorbed in the scintillator, the depth-dependent function $\zeta(z)$ is introduced. The number of collected photons at the base of the scintillator can now be written as

$$N_{collect}(z, \theta, \phi, E) = \zeta(z)N_{opt}(z, \theta, \phi, E). \quad (4.6)$$

An approximate functional form of $\zeta(z)$ was found by Freed, Park and Badano [7], by comparing with results of simulations. It was found that $\zeta(z)$ can be approximated as a linear function,

$$\zeta(z) = b_0 + b_1 z. \quad (4.7)$$

The Depth-dependent Spatial Spread

The spatial spread of the optical photons is not modelled explicitly by Freed, Park and Badano [7]. Instead, the functional form of the spread is found by performing a curve fit to results of simulations. This simplification will, of course, affect the correctness of the model. Nevertheless, a more complex model would require more knowledge about the scintillator structure.

Three different functional forms were tested by Freed, Park and Badano, namely an exponential, a Gaussian and a Lorentzian. It was found that the Lorentzian function matched the results of the simulations better than the other two. However, in these investigations, all three functions will be kept and evaluated, through experiments.

The notation $S(x, y, z)$ will be used to denote the spread, where z is the absorption depth. The two-dimensional exponential function can be written

$$S_{exp}(x, y, z, \theta, \phi) = \exp\left(-\frac{\sqrt{(x - z \tan \theta \cos \phi)^2 + (y - z \tan \theta \sin \phi)^2}}{\sigma}\right), \quad (4.8)$$

where σ determines the width of the spread. The function is symmetric around the point of absorption, $(x_0, y_0) = (z \tan \theta \cos \phi, z \tan \theta \sin \phi)$. For a material of cubic crystal lattice, such as CsI:Tl, the emission of optical photons is isotropic [6]. Therefore, the assumption of symmetry can be assumed to be valid.

Similarly, the Gaussian shaped spread can be written as

$$S_{Gauss}(x, y, z, \theta, \phi) = \exp\left(-\frac{(x - z \tan \theta \cos \phi)^2 + (y - z \tan \theta \sin \phi)^2}{\sigma^2}\right), \quad (4.9)$$

and the Lorentzian can be written as

$$S_{Lor}(x, y, z, \theta, \phi) = \frac{1}{1 + \frac{1}{\sigma^2} [(x - z \tan \theta \cos \phi)^2 + (y - z \tan \theta \sin \phi)^2]}. \quad (4.10)$$

In a final assumption, the width of the spread is approximated as a linear function of the depth,

$$\sigma(z) = g_0 + g_1 z. \quad (4.11)$$

Note that the spread has to be normalized, so that changing the width does not change the total response signal. This means that we have to divide all spread functions by $\sigma(z)^2$.

4.1. AN ANALYTICAL MODEL OF THE SCINTILLATOR RESPONSE

4.1.2 Resulting Point Spread Function

The final, analytical expression for the depth-dependent PSF is obtained by putting together the expressions, derived above. We arrive at

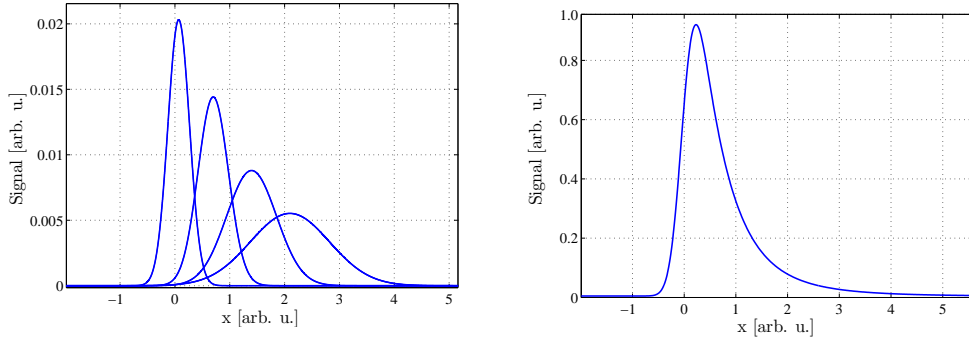
$$PSF_z(x, y, z, \theta, \phi, E) = E\mu_{PE}(E) \exp\left(-\frac{\mu_{tot}(E)z}{\cos\theta}\right) (b_0 + b_1 z) \frac{S(x, y, z, \theta, \phi)}{\sigma(z)^2}, \quad (4.12)$$

where $S(x, y)$ is one of the functions given in eqs. 4.8-4.10, and where σ is approximated as a linear function of the depth, according to eq. 4.11.

According to eq. 4.1, we integrate the depth dependent function over z , to get our total PSF.

$$PSF(x, y, \theta, \phi, E) = \int_0^{z_{max}} E\mu_{PE}(E) \exp\left(-\frac{\mu_{tot}(E)z}{\cos\theta}\right) (b_0 + b_1 z) \frac{S(x, y, z, \theta, \phi)}{\sigma(z)^2} dz. \quad (4.13)$$

Despite the symmetry of the PSF, at each given z , we will still obtain an asymmetric total PSF. This is a consequence of the depth-dependent contribution at any finite incident angle. This is illustrated in Figure 4.3, showing both the depth-dependent $PSF_z(x, z)$ for some different depths, and the total $PSF(x)$. In this example, only the one-dimensional PSF is considered. In other words, y and ϕ have been set to zero.



(a) $PSF_z(x, z)$ at some different z . The shift to the right, at increasing z , is due to a large incident angle.

(b) The corresponding $PSF(x)$.

Figure 4.3: An example of how symmetric contributions to the PSF, at different depths, gives an asymmetric total result for finite incident angle. Only the one-dimensional PSF is considered in this example, i.e., y and ϕ have been set to zero.

4.1.3 Drawbacks

The model derived in section above can be very accurate, if all unknowns are properly determined. This is shown by Freed, Park and Badano [7] through comparisons with simulations and experimental results. However, the large number of unknown constants put high demands on the precision and flexibility of the experiments.

It remains to be seen whether experiments can fill the unknown gaps of the derived analytical model. Since this is not certain, some possible modifications and simplifications are discussed in the following section.

4.2 Modifications and Simplifications

Both the width of the spread function and the absolute signal from an absorption event are modelled as linear functions of z . In a comparison with experiments, it may be difficult to distinguish these two effects and hence, a simplification may be needed.

A first step can be to simply assume that the absorption of optical photons in the scintillator is small, so that the absolute signal from one absorption event is not depth-dependent. This is not a completely unreasonable assumption, since the scintillator material is selected, based on its absolute light output. Transparency is consequently an important property of the scintillator crystal.

The depth-dependent gain may instead be replaced by an energy-dependent gain, according to

$$\zeta(E) = a_0 + a_1 E. \quad (4.14)$$

This will affect the PSF in a way, similar to the depth-dependent gain, according to eq. 4.7. The advantage of this formulation is that it is easier to measure the energy-dependence, and thus distinguish it from the depth-dependent spread, according to eq. 4.11. In addition, an energy-dependent factor will implicitly take into account effects of K-fluorescence escape. This will be an improvement, compared to the original model by Freed, Park and Badano. The PSF, with this modification, can be written as

$$PSF_{Mod}(x, y, \theta, \phi, E) = \int_0^{z_{max}} E \mu_{PE}(E) \exp\left(-\frac{\mu_{tot}(E)z}{\cos \theta}\right) (a_0 + a_1 E) \frac{S(x, y, z, \theta, \phi)}{\sigma(z)^2} dz. \quad (4.15)$$

5 | Temporal Characteristics of the Detector

In an ideal detector, the response follows instantaneously after X-ray exposure. However, intrinsic properties of the components and the materials, used in the detector, cause a temporal broadening in the produced signal. This broadening may extend up to time scale of the measurements, which leads to noticeable artifacts in the resulting images. In order to make corrections in the produced images, compensating for the temporal broadening, a better understanding for the underlying mechanisms is needed.

There are two closely related concepts, characterizing the temporal response of the flat panel scintillator detector. These are the concepts of *image lag* and *ghosting*. Recent publications largely agree on their origin [19] [12] [31] [22], although a full analytical description has not yet been presented.

An informative introduction to the two concepts is e.g. given by Zhao et al. [31]. Image lag is the residual signal, generated by previous X-ray exposures, that is carried over into subsequent image frames. Ghosting, on the other hand, refers to the change in detector sensitivity, as a result of previous exposure. This principle is illustrated in Figure 5.1. Note that if only one image is taken, this will not cause any significant problems. It is mainly the sequential imaging, as in the case of the CBCT, that will exhibit these characteristics.

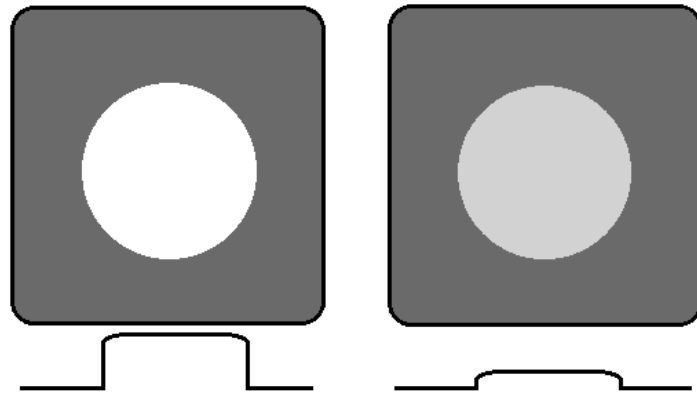
A more detailed analysis of the temporal characteristics of the detector will be presented in the rest of this chapter. An understanding of the underlying physics, as well as published empirical results will provide a basis for a model, applicable to objective of this theses.

5.1 Image Lag

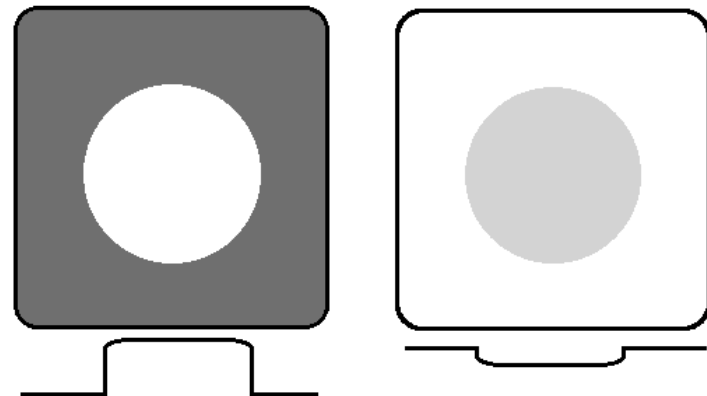
Concerning the image lag of indirect flat panel detectors, three sources are typically regarded [19]:

1. Finite decay time in the optical emission in the X-ray converter (scintillator).
2. Incomplete charge transfer of the signal, stored in the sensing element, to the read-out electronics.

CHAPTER 5. TEMPORAL CHARACTERISTICS OF THE DETECTOR



(a) Image lag: After exposure of a certain part of the detector (left), a weak residue image is present in subsequent dark images (right).



(b) Ghosting: A change in detector sensitivity, after previous exposure. In this example the initially exposed part of the detector (left) shows a decrease in sensitivity in a subsequent image (right).

Figure 5.1: An illustration of the principles of image lag and ghosting.

3. Trapping and detrapping of charge carriers in the sensing element (photodiode).

The first source depends on the properties of the X-ray converter, which in this case is a CsI:Tl scintillator. In Chapter 3, the decay time of CsI:Tl was given to be about $1 \mu\text{s}$, which can be considered as instantaneous in this context. The exposure time is normally in the order of 10 ms, which is 10^4 times the decay time.

The second and third source may be of greater importance to this analysis and will be looked into in more detail.

5.1. IMAGE LAG

5.1.1 Incomplete Charge Transfer

The speed of which charge is transferred, from the sensing element to the read-out electronics, depends the discharge time of the sensing element [8] and perhaps also the charge amplifier.

As described in Chapter 3, the sensing element acts as a capacitor, with capacitance $C_{pd} = \epsilon_r \epsilon_0 A / d$. In the read-out process, the capacitance is discharged during a finite time, that will be denoted T_{read} . Assume that the stored charge is Q_0 . It is easy to show that the discharge current from a capacitor is exponentially decaying, according to

$$I(t) = \frac{Q_0}{\tau_{RC}} e^{-t/\tau_{RC}}, \quad (5.1)$$

where the time constant is $\tau_{RC} = R_{on} C_{pd}$ and t is the time after initiating the discharge. Here, R_{on} is the resistance of the TFT in the on state. By integrating this current over the read-out time, the total charge, transferred from the photodiode, Q_{out} , is obtained,

$$Q_{out} = \int_0^{T_{read}} \frac{Q_0}{\tau_{RC}} e^{-t/\tau_{RC}} dt = Q_0 (1 - e^{-T_{read}/\tau_{RC}}). \quad (5.2)$$

The charge left on the sensing element is thus equal to $Q_0 e^{-T_{read}/\tau_{RC}}$. This will give a response in subsequent read-outs, exponentially decaying with the number of frames, n . The charge left on the photodiode after n frames can be written

$$Q_n = Q_0 e^{-n T_{read}/\tau_{RC}}. \quad (5.3)$$

An Estimation of the Time Constants

As seen in eq. 5.3, the magnitude of the lag due to incomplete charge transfer, depends on the ratio T_{read}/τ_{RC} . A quick estimation of the RC time constant can be made, using standard values of the thickness and area of the photodiode, and a typical TFT resistance. With a thickness of 1 μm , an area of 0.2mm \times 0.2mm and a TFT resistance of 1 M Ω , the RC time constant becomes roughly 4 μs . Similar values have been verified for various detector types [8] [2].

A rough value of the read-out time can also be estimated. With 10 frames per second (fps) and 2000 read-out lines, a maximum read-out time is about 50 μs . Although higher than the RC-constant, the two are definitely comparable.

5.1.2 Charge Trapping and Detrapping

The trapping and detrapping of charge carriers has been pointed out as the main source of image lag in amorphous semiconductor detectors [19] [31]. The exact kinematics of the charge carriers is complicated and depends on the distribution of trapping energies, trapping and detrapping times, level of occupancy for all different

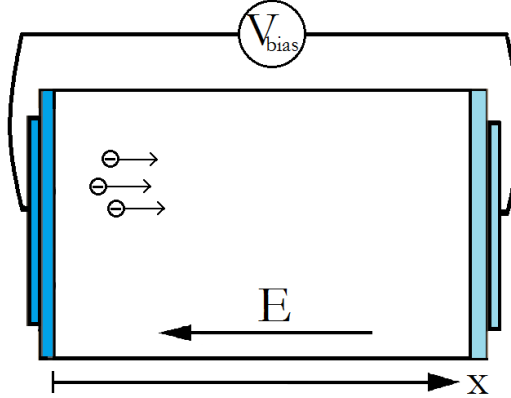


Figure 5.2: Charge trapping in the intrinsic layer of the photodiode.

traps, previous exposure, etc. An exact solution to this problem has not been presented.

Nevertheless, simplifying assumptions may allow for general analytical solutions, with validity depending on the specific circumstances. A review of suggested models is presented here.

The Hecht Equation

In 1932, Hecht [10] proposed an equation for the charge collection efficiency, in the case of a uniform electric field, E .

$$Q = Q_0 \frac{\mu_D \tau E}{d} [1 - \exp(-d/\mu_D \tau E)] \quad (5.4)$$

τ and μ_D are the trapping time and the electron mobility, respectively, and d is the length of the material, over which the field is applied.

The Hecht equation (5.4) takes into consideration the trapping of electrons, during transport, but not their subsequent release and delayed contribution to the current. Hence, it is not sufficient to describe the lagging current, present in these types of detectors.

Single Traps and Uniform Field

In a paper from 1968, Zanio et al. [30] investigated the kinematics of charge carriers in a semiconductor device, in the presence of deep traps. A simplified model was given and the resulting kinematic equations were solved analytically.

The model describes a delta pulse of charge carriers, injected into a plane-parallel semiconductor and transported through the material by an applied electric field, E . The distance from one side of the semiconductor is denoted x and the charge is assumed to be injected in $x = 0$ (see Figure 5.2). This setup is shown in Figure 5.1. Four crucial assumptions were made.

5.1. IMAGE LAG

1. Constant electric field through the device.
2. The diffusion current is negligible compared to the field current.
3. Only one type of trap.
4. The density of trapped charge is negligible compared to the density of unoccupied traps.

With these assumptions, the equations describing the density of free ($n(x, t)$) and trapped ($n_T(x, t)$) charge carriers can be written as

$$\frac{\partial n(x, t)}{\partial t} = -\mu E \frac{\partial n(x, t)}{\partial x} - \frac{\partial n_T(x, t)}{\partial t}, \quad (5.5)$$

$$\frac{\partial n_T(x, t)}{\partial t} = \frac{n(x, t)}{\tau_T} - \frac{n_T(x, t)}{\tau_D}, \quad (5.6)$$

where μ is the carrier mobility, τ_T is the trapping time and τ_D the detrapping time. Using the boundary condition of a delta pulse of charge, $N_0\delta(x)$, injected at $t = 0$, these coupled differential equations can be solved analytically. For times larger than the transit time, $t > t_{tr} \equiv \frac{L}{\mu E} \approx 10^{-12}$ s, the solution is

$$n(z, t) = \frac{\xi I_1(\xi)}{2(t-z)} \exp\left(-\frac{t-z}{\tau_D} - \frac{z}{\tau_T}\right), \quad (5.7)$$

where $z \equiv \frac{x}{\mu E}$, $\xi \equiv 2\left(\frac{\tau_T z(t-z)}{\tau_D \tau_T}\right)^{1/2}$ and $I_1(\xi)$ is the first order modified Bessel function.

To find the transient current, this expression has to be integrated over the thickness of the device, L . This gives

$$I(t) \propto \int_0^{L/\mu E} \frac{\xi I_1(\xi)}{2(t-z)} \exp\left(-\frac{t-z}{\tau_D} - \frac{z}{\tau_T}\right) dz. \quad (5.8)$$

This expression is quite complicated and difficult to deal with. One suggested simplification is to assume that the transit time is much smaller than the trapping and detrapping times ($t_r \ll \tau_D, t_r \ll \tau_T$) [30]. The expression in eq. 5.7 simplifies to a simple exponential dependence,

$$n(z, t) \propto \frac{x}{L^2} e^{-t/\tau_D}, \quad (5.9)$$

and the transient current becomes

$$I(t) \propto \int_0^L \frac{x}{L^2} e^{-t/\tau_D} dx = \frac{1}{2} e^{-t/\tau_D}. \quad (5.10)$$

Note, finally, that this result was obtained for one type of charge carriers, e.g. only electrons. Including both electrons and holes, two separate transient currents can be considered, each characterized by specific trapping and detrapping times.

Distribution of Traps

Other, more recent, sources have reported currents decaying as a power law of the time, $t^{-\gamma}$ [15] [24] [28]. In 1975, Scher and Montroll [18] became the first to derive this result, by considering a broad distribution of traps. A stochastic model was developed, which describes the kinematics of the charge carriers as a time-dependent random walk. The time-dependence was introduced through the characteristic hopping time distribution, $\psi(t)$.

The general results were interpreted and analysed by Tiedje and Rose [26] for the case of disordered semiconductors and an exponential distribution of traps. The problems associated with a broad distribution of trapping and detrapping times can be cleverly avoided, by realizing that there should be a peak in the electron distribution at a certain trapping energy, E . Since more loosely trapped electrons have shorter detrapping times, this peak energy should decrease with time. Using this time dependent trapping energy, $E(t)$, the problem can be considered as one with just a single trap.

Scher and Montrol, as well as Tiedje and Rose, arrived at the following transient currents, for times smaller and greater than the transit time t_{tr} ,

$$I(t) \propto \begin{cases} t^{-(1-\alpha)} & \text{if } t < t_{tr} \\ t^{-(1+\alpha)} & \text{if } t > t_{tr}. \end{cases} \quad (5.11)$$

The constant α was shown to be between 0 and 1. Note that the transit time is very small, compared to the time between images. This makes the second expression in eq. 5.11 the interesting form for the transient current, in this context.

The singularity that occurs as the time goes to zero is not explicitly explained by either Scher and Montrol or Tiedje and Rose. Experimental results show that the relation holds at least for times down to the order of $10^{-2} \cdot t_{tr}$ [18].

In the papers cited above, only one type of charge carrier was studied. It may therefore be of interest to extend this model, by including one term for electrons and one for holes. The two terms will have individual and unknown amplitude and decay constant α .

5.1.3 An Empirical Model of Image Lag

In 1999, Siewerdsen and Jaffrey [19] concluded, after empirical measurements, that image lag was a function of number of frames after exposure, n , rather than time. The detector, studied by Siewerdsen and Jaffrey, was an indirect flat panel detector, with a $\text{Gd}_2\text{O}_2\text{S}:Tb$ scintillator and a-Si:H sensing element.

In the following years, other authors [12] published similar results. A model, containing two exponentials, decaying with the number of frames, was used to describe the transient signal,

$$I(t) \propto C_1 \exp\left(-\frac{n}{P_1}\right) + C_2 \exp\left(-\frac{n}{P_2}\right), \quad (5.12)$$

5.2. GHOSTING

where C_1 , C_2 , P_1 and P_2 are constants that were fitted to the measured results.

Charge trapping was generally assigned as the main source of this lag, but no further explanation of this specific form of decay was given. From arguments presented earlier in this chapter, it is easy to suspect that incomplete charge transfer is influencing this kind of lagging signal. Another explanation can be that the read-out process is causing trapped charge to be released, resulting in a transient signal proportional to the amount of trapped charge. This would also lead to an exponential decay, as a function of the number of frames.

5.2 Ghosting

Ghosting is here referred to as the change in detector sensitivity, as a result of previous exposure. This will result in a multiplicative gain in subsequent images. Both increasing and decreasing sensitivities have been measured, up to the order of 10% [19].

Sources agree that ghosting depends on charge trapping in the bulk semiconductor [31] [23] [15] [13]. The effects can take on different forms, depending on the specific mechanisms involved. Recombination of charge carriers in the semiconductor can decrease the sensitivity after high exposures. On the other hand, saturation of the trapped states would allow more charges to travel through the material without being trapped, thus increasing the signal.

5.2.1 Recombination of Charge

As shown by Zhao et al. [31], the recombination of free holes and trapped electrons is the main contributor to ghosting effects in direct amorphous selenium (a-Se) detectors. This leads to a decrease in sensitivity after a high dose exposure.

Considering free holes and trapped electrons, the rate of recombination can be described by

$$\frac{dp}{dt} = -C_r p n_t, \quad (5.13)$$

where p is the concentration of holes, n_t is the concentration of trapped electrons and C_r is a constant. Assuming that n_t is constant in time, this can easily be solved, giving the concentration of holes as a function of the time

$$p(t) = e^{-C_r n_t t}. \quad (5.14)$$

The total recombined charge is thus proportional to $e^{-C_r n_t T}$, where T is the time that the holes travel through the device.

Diodes in indirect detectors are in the order of 1 μm thick, whereas direct detectors are in the order of 100 μm thick. The time of transport in the device should thus be about two orders of magnitude smaller in indirect detectors. According to eq. 5.14, this would give a vanishing recombination, compared to the case of direct detectors.

The conclusion of negligible charge recombination in indirect detectors is also drawn e.g. by Street [24] and Wieczorek [28].

5.2.2 Saturation of Trapped States

In indirect detectors, an increase in sensitivity is more common [12] [15]. This can instead be explained by the significant level of occupancy in the trapped states, that follows from high exposure [15]. This decreases the fraction of created charge carriers being trapped in subsequent signals, thus increasing the response. A proper model describing this effect is, to the author's knowledge, yet to be published.

5.3 Modelling the Temporal Response

The results of the theoretical investigations above, suggest that a model of the temporal response of the detector should contain two parts, one describing the image lag and one considering the detector gain due to ghosting. It is not certain that both models are needed to adequately describe the response of the detector studied here. Experiments will have to determine whether both effects are present and to what extent.

5.3.1 Suggested Image Lag Models

A few different models of image lag, were described in this chapter. They result in delayed signals, decaying as functions of either time, t , or frame number, n .

All models will be assumed to give a lag proportional to the incoming signal. (The validity of this will be checked experimentally.) Let the incoming signal at $t = n = 0$ be denoted S_0 . The resulting lagging signal in subsequent frames can thus be written

$$I(n, t) = S_0 \cdot L(n, t), \quad (5.15)$$

where $L(n, t)$ is the dimensionless image lag function. Note also that since $L(n, t)$ does not depend on the incoming signal, contributions from subsequent pulses can be added linearly. Table 5.1 summarizes the different forms of the function $L(n, t)$, suggested by the models described above. It also states whether they predict a dependence on t or n .

Model	$L(n, t)$	Dependence
Incomplete charge transfer	$Ce^{-\tau n}$	n
Empirical [12] [19]	$C_1 e^{-\tau_1 n} + C_2 e^{-\tau_2 n}$	n
Zanio et al. [30]	$Ce^{-\tau t}$	t
Scher and Montroll [18]	$Ct^{-\gamma}$	t

Table 5.1: A summary of the suggested models of image lag, described in Section 5.1. The form of the image lag function L is given and the dependence on time, t , or frame number, n , is specified.

5.3. MODELLING THE TEMPORAL RESPONSE

The two last models in table 5.1, can be extended to include both electrons and holes. In that case, two similar terms can be used, with constants that should be determined individually.

5.3.2 A New Ghosting Model

Following the hypothesis that ghosting depends on charge trapping, a simplified model can be drafted. This model will describe a gain in detector sensitivity, due to a significant occupation of the trapped states in the a-Si:H.

Denote the fraction of occupied traps $n(t)$. Assume that the traps are filled at a rate proportional to the fraction of unoccupied traps, $1 - n(t)$, and the intensity of the incoming signal, $S(t)$. Similarly, assume that charge is released at a rate proportional to the number of occupied traps. The change in $n(t)$ can then be written

$$\frac{dn(t)}{dt} = \frac{S(t)}{\tau_T}(1 - n(t)) - \frac{n(t)}{\tau_D}, \quad (5.16)$$

where the first term on the right hand side is due to trapping and the second term is due to detrapping. τ_T and τ_D are, once again, trapping and detrapping constants. The detected current at time t can now be written as

$$I(t) = S(t) \left(1 - \frac{C}{\tau_T}(1 - n(t)) \right) + C \cdot \frac{n(t)}{\tau_D}, \quad (5.17)$$

where C is some unknown constant.

Note that the last term in eq. 5.17 is due to detrapped charge, in other words, image lag. This model is supposed to describe the effects of ghosting and hence this last term is dropped.

Assume that there is no trapped charge at $t = 0$, i.e., $n(0) = 0$. The gain, $G(t)$, due to ghosting can be written as the fraction

$$G(t) = \frac{I(t)}{I(0)} = \frac{1 - \frac{\text{const}}{\tau_T}(1 - n(t))}{1 - \frac{\text{const}}{\tau_T}} = 1 + \frac{\text{const}}{\tau_T - 1}n(t). \quad (5.18)$$

Defining a new constant $D \equiv \frac{\text{const}}{\tau_T - 1}$, the gain can be written as

$$G(t) = 1 + D \cdot n(t). \quad (5.19)$$

In this model, the fraction of occupied traps, $n(t)$, is determined by the differential eq. 5.16. The constants τ_T, τ_D and C have to be determined experimentally.

6 | Experimental Methods

In Chapters 4 and 5, a model for the response of the X-ray scintillator detector was developed. The model takes into consideration the spatial spread, due to optical transport in the scintillator, as well as the temporal characteristics of the active matrix array.

Because of insufficient information about the exact properties of the detector, several parameters had to be considered unknown. This concerns both the temporal response of the detector and the spatial spread. To determine the missing parameters and to check the validity of the derived models, experimental measurements are required.

The purpose of this chapter is to describe the set-up of the experiments, carried out to determine the missing pieces of the response model. The results and conclusions drawn from the experiments will be presented in succeeding chapters.

6.1 Detector Set-up and Limitations

A complete CBCT system is set up, in connection to a Leksell Gamma Knife, at one of Elekta's demo sites. As described in Chapter 1, the CBCT scanner consists of the X-ray source (X-ray tube) and the detector, attached to a gantry, which allows the system to rotate roughly 200° around an object. The scanner is controlled by software, which is currently under development. This means that the designing of experiments is limited by the features of the current software release.

6.1.1 Experimental Parameters

Basically, the system is built to perform CBCT scans, where the source and the detector rotates around an object, taking several images each second. The source will produce pulses of cone shaped beams, reaching all parts of the detector.

The parameters that allow manipulation are the number of frames per scan, the frame rate, the peak kilovoltage (kVp) and the charge used to produce a pulse of X-rays in the X-ray tube. The latter is chosen by entering a pulse length and a current. The unit commonly used to describe the total charge is milliampere-seconds (mAs). The limitations on each parameter are described in table 6.1.

CHAPTER 6. EXPERIMENTAL METHODS

Parameter	Min	Max
Frame rate [Hz]	0	11.6
kVp	40	120
Charge used in source [mAs]	0.1	1.6

Table 6.1: Experimental parameters and their possible manipulation.

In addition to these parameters, the detector has three different sensitivity settings. These are denoted G3, G4 and G5, with G3 being the highest sensitivity. It is not specified exactly how they are implemented, but presumably, the electrical signal from the active matrix is amplified by certain factors, corresponding to each of the three settings.

6.1.2 X-ray Spectra

It is generally of great importance to take into consideration the energy spectra emitted by the X-ray source. This concerns mainly the spatial response of the detector, since the energy of the X-ray affects how far it penetrates the scintillator before being absorbed and converted into optical photons. One possible way to obtain the spectra is through detailed simulations of the electrons and photons in the X-ray tube.

Elekta has previously developed an advanced multi-purpose Monte Carlo simulation tool, called PEGASOS. The physics engine in PEGASOS is based on the PENELOPE package, released by the OECD Nuclear Energy Agency (NEA) [14]. Using this tool, Elekta has simulated energy spectra, produced by the X-ray tube. One spectrum requires the simulation of at least $5 \cdot 10^{10}$ initial particles (electrons), with the use of variance reduction techniques to further increase the efficiency. This procedure takes a few days to run on a 56 node cluster. Therefore, only a limited number of spectra have been simulated, namely those corresponding to 40, 70, 80, 90, 100, 110 and 120 kVp.

There are algorithms that can generate the energy spectra for a range of kVps. In [21], Siewerdsen et al. present a computational tool called Spektr. This tool offers the convenient calculation of X-ray spectra of tungsten X-ray tubes, as well as the calculation of beam quality characteristics in a large selection of elements and compounds. The spectra given by Spektr are not as detailed as the ones computed using PEGASOS simulations. But apart from the difference in resolution, the normalized spectra coincide quite well. This is demonstrated in Figure 6.1. In order to better visualize the similarities and differences, the detailed PEGASOS spectra have been down-sampled, through a convolution with a triangular pulse. This is shown in red, in the plots.

The normalized spectra have to be multiplied by a factor, corresponding to the number of produced X-ray photons per charge. This step is crucial in order to compare the measured signals at different kVp. The factors, as given by the PEGASOS simulations, are shown in Figure 6.2.

6.1. DETECTOR SET-UP AND LIMITATIONS

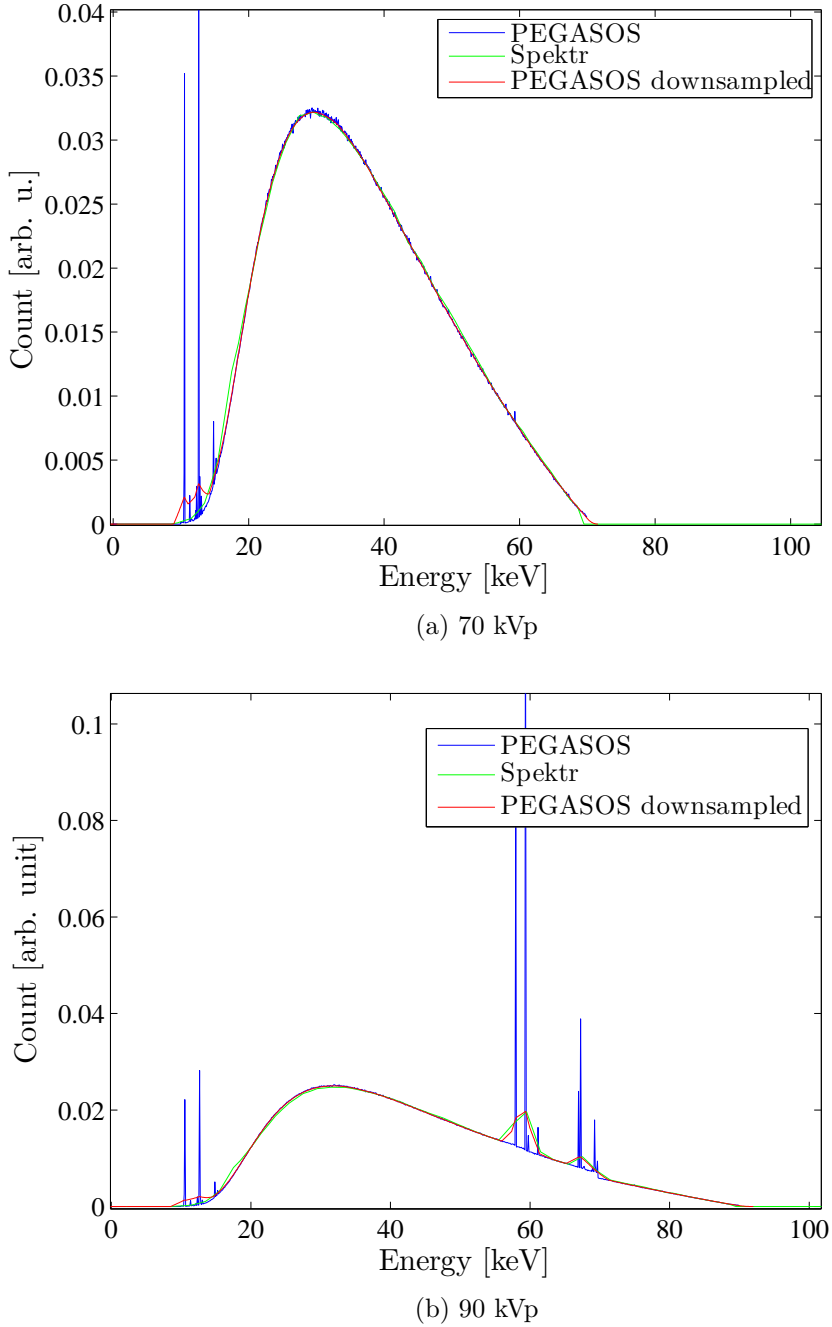


Figure 6.1: A comparison of X-ray tube spectra, obtained through detailed Monte Carlo simulations in PEGASOS and the simpler algorithm called Spektr. The PEGASOS spectra (blue) have been convolved with a triangular pulse (red), in order to better visualize the similarities and differences with the spectra, generated by Spektr (green).

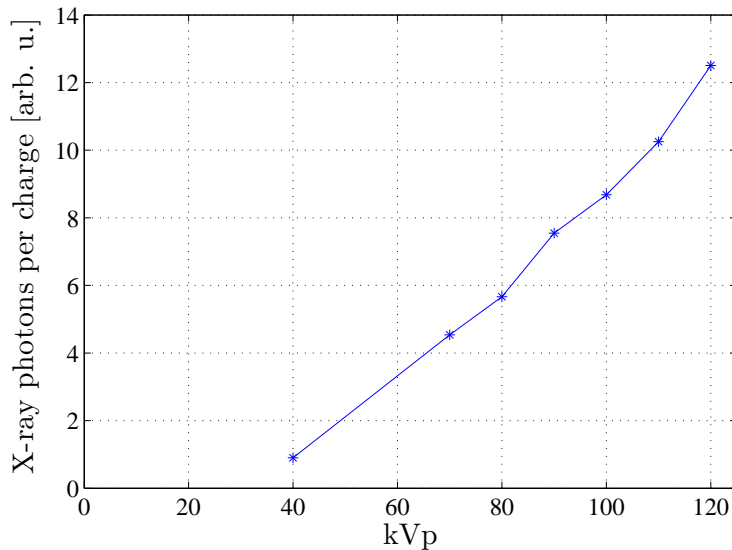


Figure 6.2: The number of X-ray photons produced in the X-ray tube per charge, as a function of kVp.

6.1.3 Filters

In addition to the manipulation of the experimental parameters, described above, filters can be used to adjust the X-ray intensity. These are placed in connection to the X-ray tube, blocking the path of the produced beam. Commonly used filters are flat plates of aluminium or copper.

In CBCT scans of the head, it is common to use a so called *bowtie filter*. The name refers to the actual shape of the metal, which is attached to the X-ray tube. This will result in an X-ray intensity, which is highest in the center of the detector, and gradually decreases towards the edges.

An interesting use of the bowtie filter is that it conveniently varies the X-ray intensity across the detector, thus decreasing the number of scans needed to achieve a complete set of experimental parameters. One should remember, however, that the use of any filter will modify the incident X-ray spectra.

6.2 Measuring the Point Spread Function

In order to directly measure the PSF, a number of requirements have to be met. Most importantly, the X-rays have to be incident on the detector in a single point. Unfortunately, this is not possible to achieve with the available equipment. Instead, a measurement over a sharp edge can provide similar information about the spatial spread of the response. The measured function will be referred to as the *edge spread function*.

6.2. MEASURING THE POINT SPREAD FUNCTION

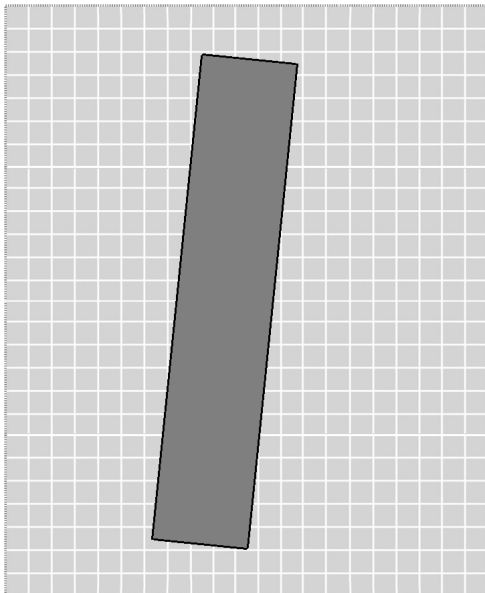
6.2.1 Measuring the Edge Spread Function

Using a plate of highly attenuating material, a sharp edge can be obtained, between full exposure and complete blocking of the incident X-rays. For this purpose we will use a $5 \times 25 \times 300 \text{ mm}^3$ plate of tungsten copper alloy. This material has high density and attenuates effectively all incident X-rays up to about 150 keV.

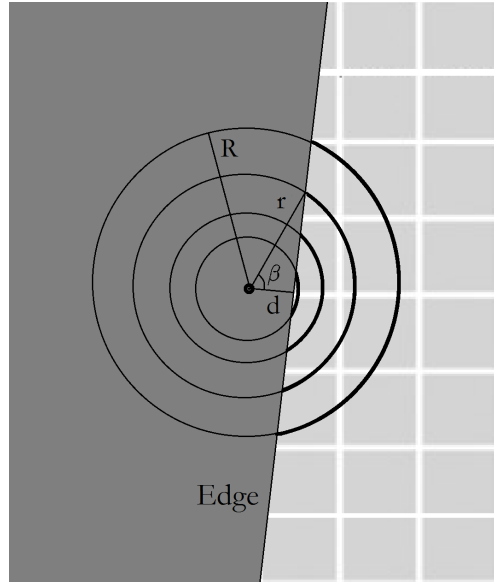
The width of the PSF will not be larger than in the order of a pixel. A broader response would blur the image to the point where the high number of pixels would be completely redundant. This means that the signal over the edge of the plate will be measured with very low resolution.

A higher resolution can be attained by adding together the curve at many different points along the edge. If the plate is placed such that the edge is slightly tilted over the pixel matrix (see Figure 6.3a), the resulting curves will be slightly displaced, thus together providing detailed information about the shape of the curve.

This concept is further visualized in Figure 6.4. The first plot shows the signal over the edge at a single pixel row. In the second plot, hundreds of similar curves, from all parts of the edge, have been put together in a single plot. One can clearly see how the different curves contribute to giving a high resolution result of the signal.



(a) The CuW plate is placed diagonally across the pixel matrix.



(b) The contribution from the unblocked detector, up to some maximum distance, is integrated.

Figure 6.3: The set-up of the edge spread measurement. Note that the size of the plate, compared to the pixels, is not to scale.

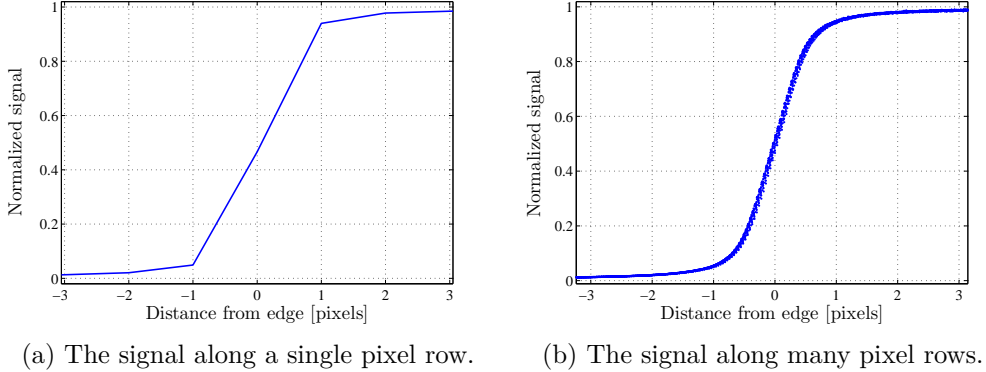


Figure 6.4: An illustration of how the measured signal across the edge, along many different pixel rows, can be used to produce a curve of sub-pixel resolution.

6.2.2 Comparison with Analytical Models

In order to compare the measured edge spread function to the derived model, one first has to derive the edge spread function from the PSF. This is done by summing up the contribution from all unblocked parts of the detector, within a certain maximum distance.

One way of doing this is to take the PSF and integrate over the distance to the unblocked parts of the detector, according to Figure 6.3b. The procedure is repeated for each point along the edge spread function. The integral is taken from the distance to the edge, d , to some maximum distance, R , where the contribution is virtually zero. For each distance, r , the contribution from the PSF has to be weighted by the arc length, which is proportional to the angle $\beta = \arccos(r/d)$, according to the figure.

When this is done, the calculated function can be compared to the measured results, thus checking the validity of the model.

6.2.3 An Energy-dependent Factor

As discussed in Section 4.2, the many unknown constants of the PSF, according to eq. 4.13, will be difficult to determine. Instead, the PSF can be assumed to have a form according to eq. 4.15, which contains the energy-dependent factor

$$\zeta(E) = a_0 + a_1 E. \quad (6.1)$$

This factor can be determined independently from the rest of the PSF, by measuring the signal value from the detector, at a range of different kVps. The total signal, according to this model of the PSF will be

$$I = \int_E \text{spectrum}(E) dE \int_0^{z_{max}} E \mu_{PE}(E) \exp\left(-\frac{\mu_{tot}(E)z}{\cos(\theta)}\right) (a_0 + a_1 E) dz. \quad (6.2)$$

6.3. MEASURING THE TEMPORAL RESPONSE

Note that the integration over the energy spectrum has been included in the expression. By comparing this to the experimental data, the constants a_0 and a_1 can be determined.

6.2.4 The Scintillator Thickness

The thickness of the scintillating layer plays an important role for the spatial spread of the response, as discussed in Chapter 3. This information is not given by the manufacturer of the detector and will therefore have to be otherwise determined. Efforts were put into finding an experiment that could determine the scintillator thickness. Unfortunately, the ideas later showed to be fruitless.

However, the model derived in Chapter 4 has some ability to compensate for falsely determined parameters [7]. An approximate thickness can therefore be sufficient, since this assumption will be taken into account in the fitting of the depth-dependent spread, as well as the energy-dependent factor, to experimental results.

An approximate scintillator thickness can be estimated, partially from technical data from competing manufacturers [17] [16], and partially from standard values, used in literature [5]. The plausibility of these values can also be checked, by analysing the attenuation of X-rays in the scintillating material. As discussed in Chapter 3, the scintillator thickness is chosen as a compromise between high light output and a limited spatial spread.

An estimated scintillator thickness of $600 \mu\text{m}$ will be used in the further analysis of the PSF.

6.3 Measuring the Temporal Response

In experimental measurements of the temporal response of the detector, the average signal over a large number of pixels will be considered. Scans of many consecutive images will be used in order to determine the influence of image lag and ghosting. Note that these two effects are closely related and that a separation of the two is not trivial. To see this, consider the general case of a scan at a certain frame rate.

The frame number will, in accordance with previous chapters, be denoted n . Let the incoming signal in frame n be denoted S_n and write the detected signal as I_n . In the first frame, we will simply measure the incoming signal, i.e.,

$$I_1 = S_1. \quad (6.3)$$

According to the discussion in Chapter 5, the second frame will also detect a lagging signal from the first frame, as well as a gain, G , due to the previous exposure. This can be written as

$$I_2 = S_2 \cdot G(S_1) + S_1 \cdot L(1). \quad (6.4)$$

Here, the image lag is written as a function of the frame number. Whether this is really due to a time dependence is not important for the notation, at this point.

CHAPTER 6. EXPERIMENTAL METHODS

In frame n , the signal will depend on all previous exposure, according to

$$I_n = S_n \cdot G(S_1, \dots, S_{n-1}) + S_1 \cdot L(n-1) + \dots + S_{n-1} \cdot L(1). \quad (6.5)$$

Eq. 6.5 describes a very general case of the temporal response, from a CBCT scan. The assumptions made so far are that the image lag is linear, as discussed in chapter 5, and that any cross terms between image lag and ghosting are negligible.

6.3.1 Flood Scan

Consider the case where all incoming X-ray pulses are of equal size. This will be the case when there is no blocking object between the source and the detector. Such a scan will here be referred to as a *flood scan*.

The signal from the detector can be described by the general formula, given in eq. 6.5. In this case, however, the indices of the incoming signal, S_n , can be dropped. This enables us to write

$$I_n = S \cdot G(S, \dots, S) + S \sum_{k=1}^{n-1} L(k). \quad (6.6)$$

Note that the ghosting and image lag are both still present in the detector response. The measured signal will have a shape, similar to the plot in Figure 6.5.

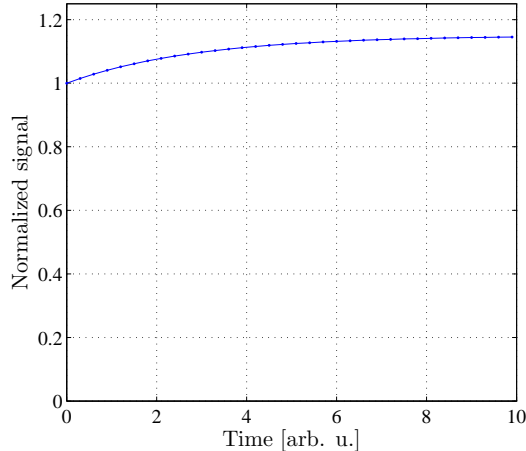


Figure 6.5: The expected result of a flood scan. The gain in the signal is due to both image lag and ghosting effects.

6.3.2 Measuring Image Lag

A separation of image lag and ghosting effects can be achieved by disabling the X-ray source during a scan, and measure the signal in the following frames. This

6.3. MEASURING THE TEMPORAL RESPONSE

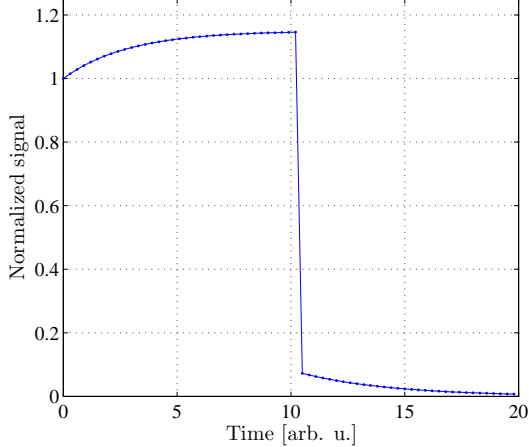


Figure 6.6: The expected result, when the X-ray source is disabled during a scan. The first half of the plot shows effects of both image lag and ghosting, whereas the signal, after the source has been disabled, is only due to image lag.

possibility is not provided by the CBCT, but can be cleverly achieved, using an inherent safety feature. The safety feature is a, so called, dead man's switch, that immediately turns off the X-ray source if the operator releases a button, which otherwise has to be pushed down throughout the scan. When the source has been turned off, the system will finish the started scan, taking images without exposure, thus producing the desired result.

Consider now a sequence, where the X-ray source is suddenly disabled, after a certain time. An ideal result of such a measurement is shown in Figure 6.6.

The numbering of the frames will now start when the source is disabled, i.e., I_n is the signal in the first frame taken without exposure. Using equation 6.6, the signal in these frames can be written

$$\begin{aligned}
 I_1 &= S \cdot (L(1) + L(2) + L(3) + L(4) + \dots) \\
 I_2 &= S \cdot (L(2) + L(3) + L(4) + \dots) \\
 &\vdots \\
 I_n &= S \sum_{k=n}^N L(k),
 \end{aligned} \tag{6.7}$$

where N depends on how many frames that were taken, before disabling the source. It is easy to see that the difference between consecutive signals (n and $n + 1$) is simply $S \cdot L(n)$. Hence, the effects of image lag can be directly measured, without the effects of ghosting.

6.3.3 Measuring Ghosting

When the image lag effect has been measured and properly characterized, it is possible to return to the results of the flood scans and separate image lag from ghosting. It is simply a matter of subtracting the last term in equation 6.6, according to

$$I_n - S \sum_{k=1}^{n-1} L(k) = S \cdot G(S, \dots, S). \quad (6.8)$$

This will isolate the gain effect, due to ghosting. The result can be compared to the model, discussed in Chapter 5.

Note that it is not known whether both image lag and ghosting effects are really present in the studied detector. Should this be the case, their relative size could still differ to the point where one dominates completely over the other. If image lag dominates over ghosting, the result according to eq. 6.8 will simply be a constant signal. In the opposite case, where ghosting dominates the image lag, the subtraction in eq. 6.8 will not make much difference at all. Three possible outcomes of this experiment are shown in Figure 6.7.

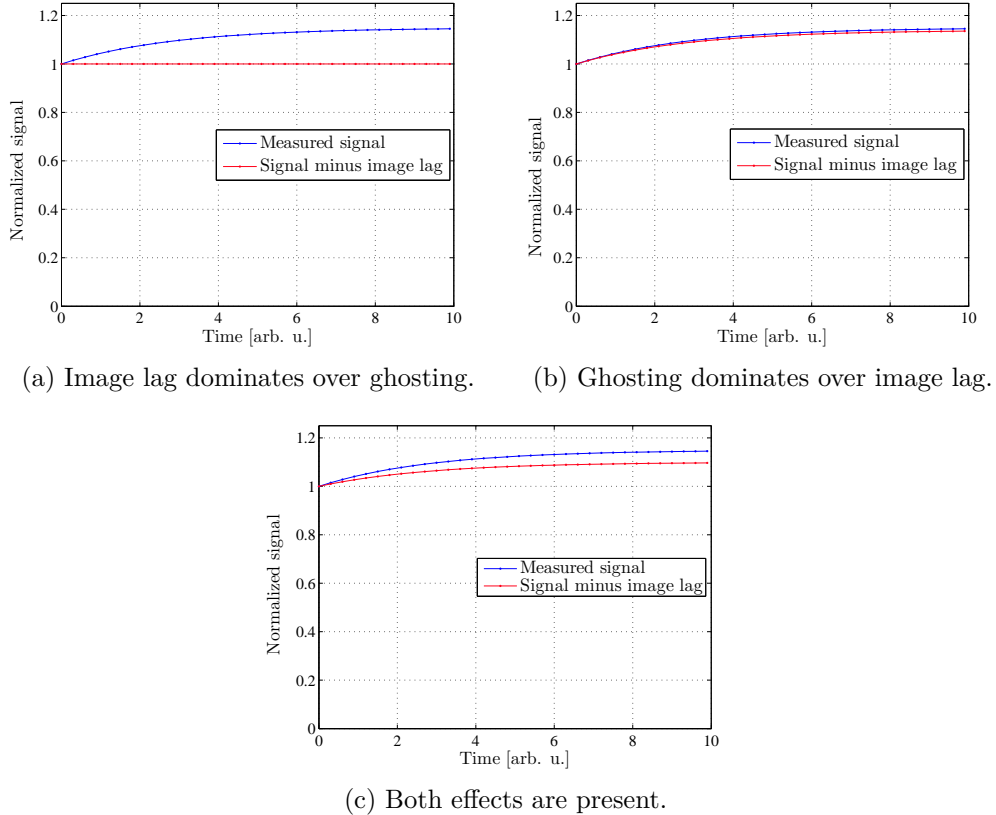


Figure 6.7: Three possible outcomes, after subtracting the image lag from a flood scan. The result will reveal the effects of ghosting.

6.3. MEASURING THE TEMPORAL RESPONSE

A Comparison to the Analytical Model

The analytical model of ghosting, derived in Section 5.3, suggests a gain according to

$$G(t) = 1 + D \cdot n(t), \quad (6.9)$$

where D is a constant. The fraction of filled charge traps at a certain time, $n(t)$, is determined by the differential equation

$$\frac{dn(t)}{dt} = \frac{S(t)}{\tau_T}(1 - n(t)) - \frac{n(t)}{\tau_D}, \quad (6.10)$$

where τ_T and τ_D are the unknown trapping and de-trapping constants.

In the case of a flood scan, the intensity of the incoming signal is constant in time, i.e., $S(t) \equiv S$. This enables us to solve eq. 6.10 analytically. Using the initial condition $n(0) = 0$, the solution becomes

$$n(t) = \frac{S}{S + \tau_T/\tau_D} \left(1 - e^{\left(\frac{S}{\tau_T} + \frac{1}{\tau_D}\right)t} \right) \quad (6.11)$$

The total gain, in the case of a flood scan, can thus be written as

$$G(t) = 1 + D \frac{S}{S + \tau_T/\tau_D} \left(1 - e^{\left(\frac{S}{\tau_T} + \frac{1}{\tau_D}\right)t} \right). \quad (6.12)$$

This equation can be used in order to relate the experimental result to the analytical model, and determine the unknown constants D , τ_T and τ_D .

6.3.4 A more Advanced Measurement Sequence

Finally, a clever measurement sequence is described, which can be used to directly measure the effects of ghosting. Unfortunately, this method is not possible to implement with the equipment available at this time. It may, however, be useful in further investigations and will be included for that reason. The basic idea is to alternate X-ray pulses with dark frames, and then subtract the underlying image lag. This is described in more detail by Overdick et al. [15].

The sequence is shown in Figure 6.8. First, a number of test shots are taken as reference values. After a while, the detector is exposed to a certain load, possibly resulting in both image lag and ghosting. Finally, alternating dark frames and test signals are measured. As seen in Figure 6.8, the underlying lagging signal can be subtracted from the measurements, revealing the effects of ghosting.

CHAPTER 6. EXPERIMENTAL METHODS

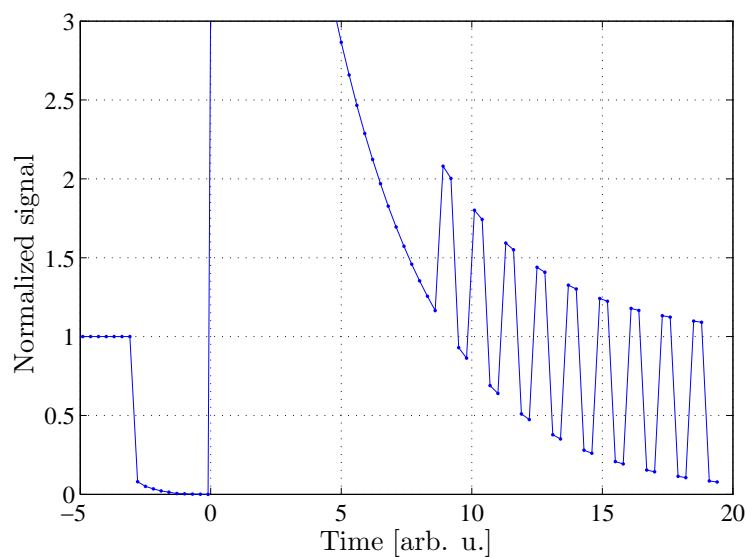


Figure 6.8: A possible measurement sequence that will isolate the gain due to ghosting. At time 0, the detector is exposed to a very high load, resulting in both image lag and ghosting effect. After that, alternating reference pulses and dark frames are used in order to separate the two effects.

7 | Results

In order to fill the gaps of the detector response model, a number of experiments were performed. The results of the experiments are presented in this chapter, together with comparisons with the suggested models.

Similarly to the structure in previous chapters, the spatial response will be treated first. After that, the results concerning the temporal characteristics of the detector are presented.

7.1 The Point Spread Function

As described in chapter 6, the PSF can be determined by first measuring the spread across a sharp edge, the so called *edge spread function*. The result can be compared to the analytical PSF, by integrating the contribution from the unblocked part of the detector.

In chapter 4, two different forms of the PSF were presented. These are given in eqs. 4.13 and 4.15, respectively. After analysing the experimental result, the second form, according to eq. 4.15, was found to be more suitable. This is mainly because it contains an energy-dependent factor, which can be determined independently of the spread. The results of the separate experiments, measuring the energy-dependent signal strength and the depth-dependent spread, are presented in this section.

7.1.1 The Energy-Dependent Factor

As previously discussed, the energy-dependent signal strength will be assumed to have the form

$$\zeta(E) = a_0 + a_1 E, \quad (7.1)$$

where a_0 and a_1 are the constants to be determined. The energy, E , will be given in keV.

Measurements were made of the average signal at the center of the detector at 40, 50, 70, 80, 90, 100, 110 and 120 kVp. Firstly, the effects of image lag and ghosting were removed, using the models discussed later in this chapter. Then, the signals were compared to the expected values, according to eq. 6.2. The best fit

constants were found to be

$$\begin{aligned} a_0 &= 1, \\ a_1 &= 0.0331 \text{ keV}^{-1}. \end{aligned} \quad (7.2)$$

In this discussion, only the signal up to a multiplicative constant is of interest. The best fit constants have therefore been normalized by setting a_0 to one.

The Sensitivity Setting

In chapter 6, it was mentioned that the detector has three sensitivity settings, G3, G4 and G5, with G3 being the highest sensitivity. Measurements at varying sensitivity showed that the detector signal is simply amplified by a certain factor, depending on this setting. Setting the factor, corresponding to G3, to one, the factors for G4 and G5 were shown to be 0.224 and 0.165, respectively. When comparing the results at different sensitivity settings, these factors have to be considered.

7.1.2 Edge Spread Function

Measurements were made of the signal across the sharp edge of a 5mm×25mm×300mm CuW plate, at 50, 90 and 120 kVp. A detailed description of the experimental set-up was given in section 6.2. The point of repeating the experiment with different energies was to achieve a varying attenuation at different depths, thus providing a more complete set of data, from which to determine the depth-dependent spread.

The analytically derived PSF was used to calculate the signal, resulting from the beams incident X-ray onto the unblocked part of the detector, up to 7360 μm away (20 pixels). Three different shapes of the PSF were tested in the comparison with the experimental data. These included a Lorentzian, a Gaussian and an exponential shape. The width of the distribution was assumed to be depth dependent, according to the detailed derivation in chapter 4.

The Shape of the Spread

The first task, in the determination of the PSF, was the finding of the functional form of the depth-dependent spread, denoted $S(x, y, z)$. Similar investigations by Freed et al. [7], showed that the Lorentzian spread gave the best fit. In that particular case, the analytical model was compared to results of simulations. In this case, however, the Lorentzian did not match the experimental result. Instead, the exponential and the Gaussian showed to be far superior. The exponential also showed a consistency between the experiments that could not be matched by any of the other two.

The best fit to the experimental edge spread is shown in Figure 7.1, for the Gaussian, exponential and Lorentzian, respectively. The displayed results were obtained for 50 kVp.

7.1. THE POINT SPREAD FUNCTION

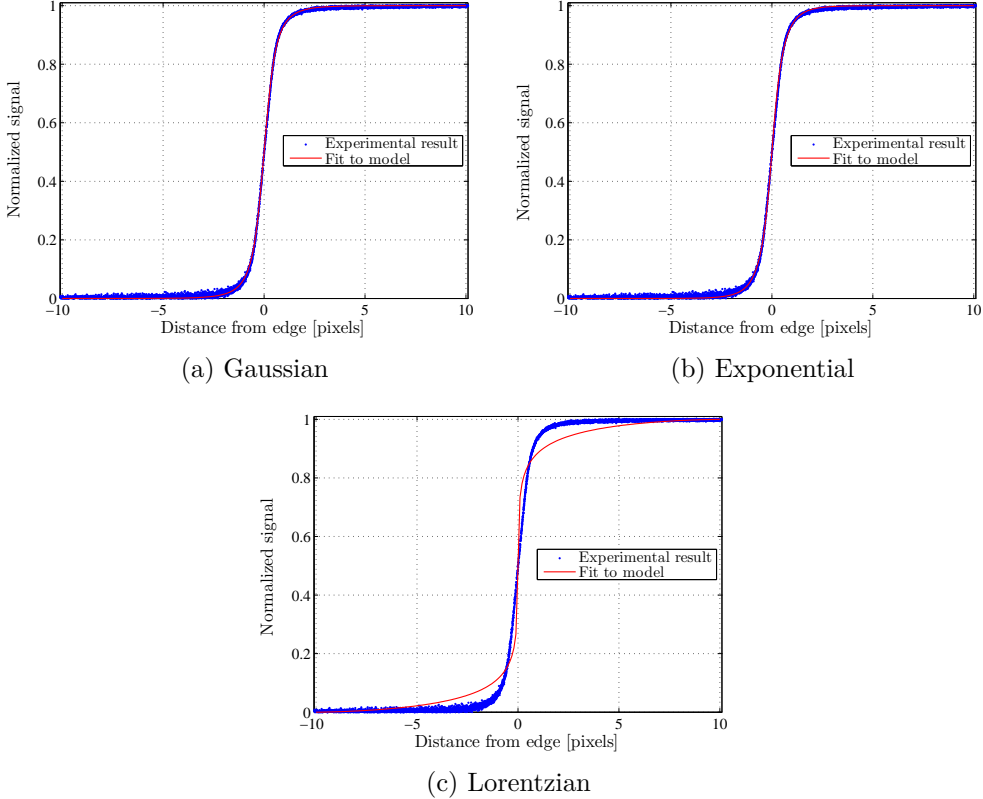


Figure 7.1: The best fits of the edge spread function, for the Gaussian, exponential and Lorentzian spread, respectively. The displayed results were obtained for 50 kVp.

The Width of the Spread

The width of the PSF, $\sigma(z)$, was approximated as a linear function of the depth, according to

$$\sigma(z) = g_0 + g_1 z. \quad (7.3)$$

The best fit constants, g_0 and g_1 were determined for each measurement and the resulting $\sigma(z)$ is shown in Figure 7.2. Only the exponential shape is considered here, since it gave the most consistent results.

The next step is to determine a compromise between the three results, to use in the final PSF. For this we can take advantage of the difference in X-ray energy, between the measurements. In the first measurement, at 50 kVp, more than half the X-ray energy is absorbed within the first 100 μm , in the scintillator. The width of the spread, at low depths, should thus be most accurately determined by this measurement.

New curve fits were made for 90 and 120 kVp, using $g_0 = 80\mu\text{m}$, which was the result for 50 kVp. It was shown that $g_1 = 0.35$ gave a result that matched all measurements fairly well. The final expression for $\sigma(z)$, with the mentioned

constants, is shown as a dashed line in Figure 7.2. The corresponding curve fits, to the experimental edge spread functions, are shown in Figure 7.3.

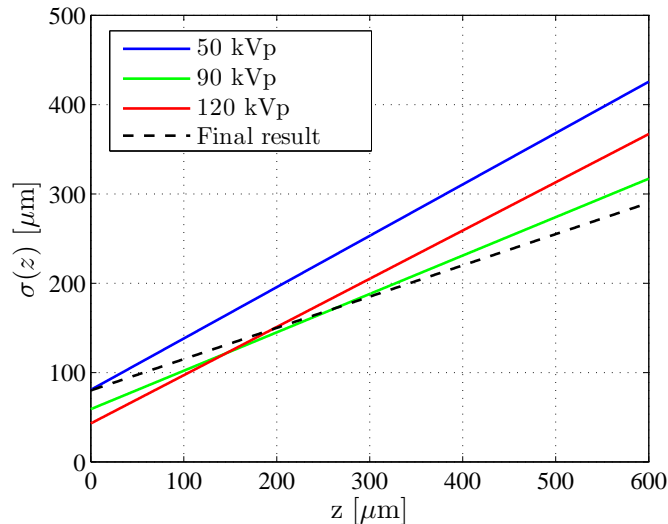


Figure 7.2: The resulting depth-dependent width, $\sigma(z)$, according to the linear approximation (eq. 7.3). The dashed line shows the function that will be taken as a final result. The results are given for the exponential shape.

7.2 Image Lag

The image lag was measured for a variety of frame rates, X-ray intensities and all three sensitivity settings. The results clearly showed a lagging signal in the dark frames following after exposure, with a striking consistency between the measurements.

The experimental set-up was thoroughly described in section 6.3.2. During the scans, the source was disabled after approximately 200 frames, and another 100 to 150 dark frames were then taken. The difference between subsequent frames, after the source had been disabled, was calculated in order to obtain the desired image lag function.

Before determining the exact form of the image lag function, two important questions from chapter 5 can be readily answered. The first question concerns whether the signal decays as a function of time or number of frames. The second question is whether the image lag is, as assumed, directly proportional to the incoming signal.

7.2.1 Time or Frame Number?

The question concerning the dependence of the image lag function can be answered by inspection of the results at different frame rates. In Figure 7.4, the normalized

7.2. IMAGE LAG

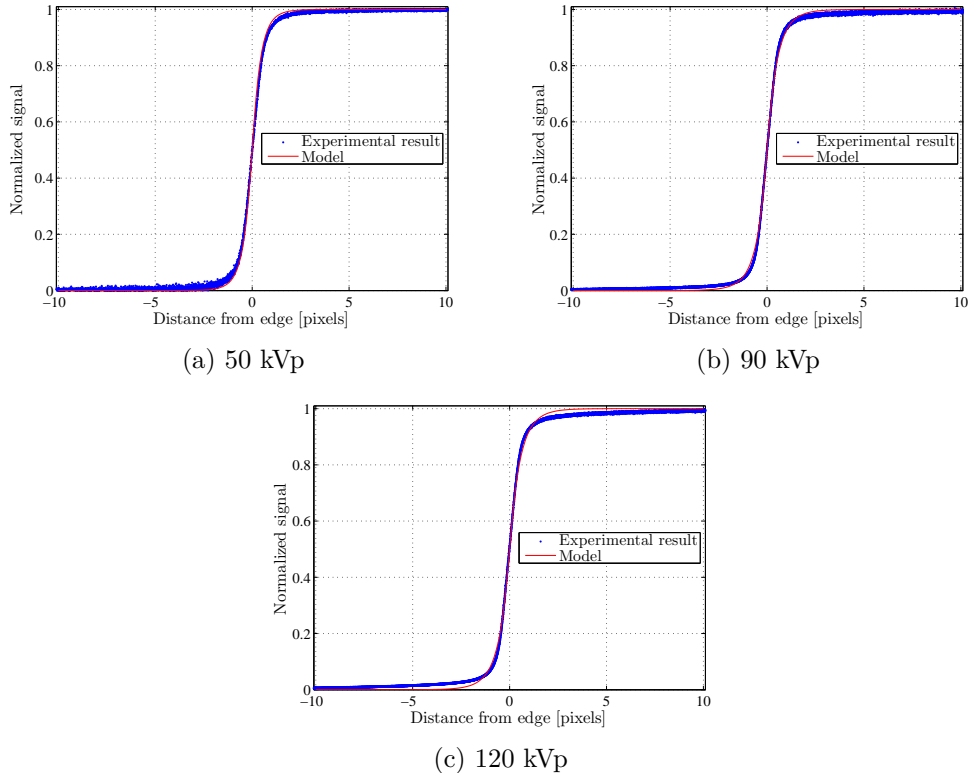


Figure 7.3: The final edge spread function, with the exponential spread, together with the experimental results at 50, 90 and 120 kVp.

image lag is shown for three different measurements, as a function of time, t , and frame number, n , respectively. The normalization was done by dividing the signal values by the value of the first frame of the scan. In each case, the detector was divided into squares of 100×100 pixels, which were considered individually.

The results clearly show that the image lag for the investigated detector decays as a function of time, and not as a function of frame number explicitly, as in the case described by Siewerdsen and Jaffrey [19].

7.2.2 Proportionality

The question of proportionality is also easily answered by inspection of the result in Figure 7.4. The normalized image lag is shown, for a variety of exposures, frame rates and sensitivity settings. Since the resulting functions coincide in all measurements, it can be concluded that the image lag, as assumed, is directly proportional to the incoming signal. Also the assumption of linearity is supported by this results.

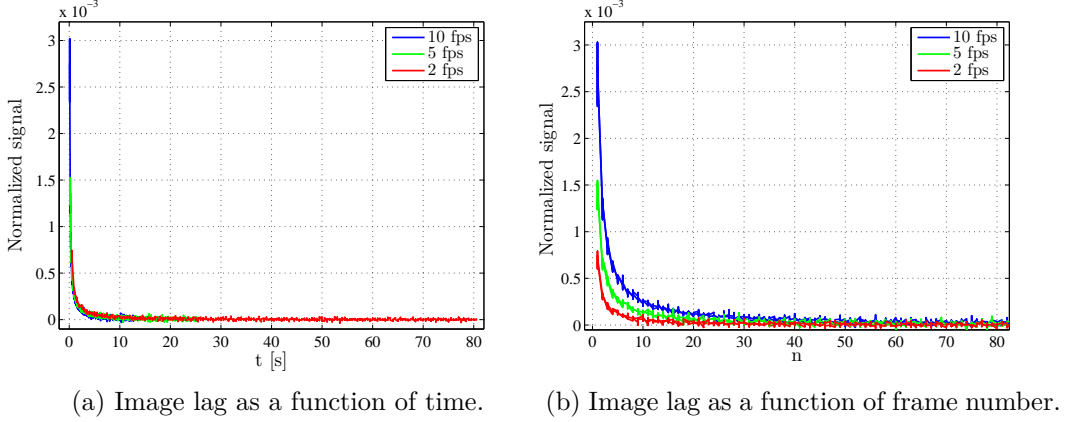


Figure 7.4: The resulting image lag, plotted as a function of time and frame number, respectively. The displayed results are from a single scan at 90 kVp and with sensitivity setting G3, but all other scans gave very similar results. The X-ray intensity was varied over the detector, using a bowtie filter.

7.2.3 The Shape of the Image Lag

With the conclusions drawn above, we can write the image lag as

$$I(t) = S_0 \cdot L(t), \quad (7.4)$$

where S_0 is the incoming signal at $t = 0$ and $I(t)$ is the measured image lag. It is now time to determine the exact shape of the dimensionless image lag function $L(t)$.

The models, suggested in chapter 5, were all fitted to the experimental curve. It was shown that the power law decay, according to,

$$L(t) = Ct^{-\gamma}, \quad (7.5)$$

was superior to the other forms. A curve fit was made for 11 separated measurements, of varying X-ray intensity, frame rate and sensitivity setting. Again, the detector was divided into squares of 100×100 pixels, which were all considered individually. The best fit constants, C and γ , from all fits were averaged, giving the numerical values

$$C = 2.53 \cdot 10^{-4} \text{ s}^\gamma, \quad (7.6)$$

$$\gamma = 1.11. \quad (7.7)$$

For the purpose of rigour, it can be noted that the image lag function should preferably be written on the form $C \left(\frac{t}{t_0} \right)^{-\gamma}$, with t_0 being a time constant with unit s. This is in order to avoid the inappropriate unit $\text{s}^{-1.11}$ for the constant C . However, this will not result in any practical differences, and the simpler form $C \cdot t^{-\gamma}$ will be kept. The data from all measurements, together with the fitted image lag function, is presented in Figure 7.5.

7.3. GHOSTING

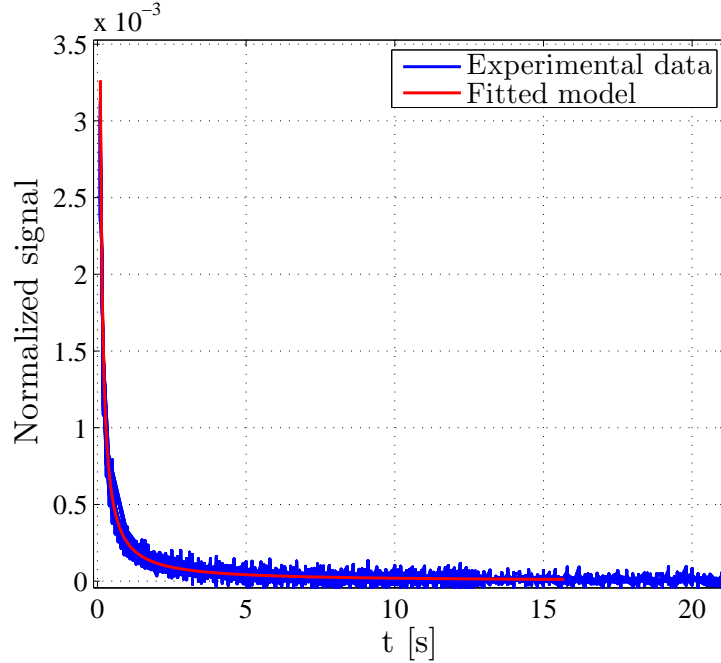


Figure 7.5: Experimental image lag as a function of time, together with a curve fit according eq. 7.5

7.3 Ghosting

After using the derived model to subtracting the image lag, the images from the flood scans still showed a significant increase in signal, with time. (The correction procedure is further described in the final section of this chapter.) This is a clear implication that image lag is not the only effect that characterizes the temporal response of the detector. The gain was shown to increase with increasing signal, in accordance with the theoretical analysis of ghosting.

7.3.1 Fitting the Experimental Results to the Derived Model

In chapter 5, a relatively simple model was derived, in order to describe the effects of ghosting due to charge trapping. In chapter 6, this model was used to calculate the gain effect due to ghosting, in the specific case of a flood scan. The resulting gain, $G(t)$, was shown to be

$$G(t) = 1 + D \frac{S}{S + \tau_T/\tau_D} \left(1 - e^{\left(\frac{S}{\tau_T} + \frac{1}{\tau_D}\right)t} \right), \quad (7.8)$$

where D , τ_T and τ_D are unknown constants and S is the intensity of the incoming signal. Note that, in this model, it is important to take into account the detector sensitivity setting, used in the measurements. The signal S refers to the actual X-

ray intensity, incident on the detector. Thus, when changing the sensitivity setting, the signal must be divided by the factors, given in section 7.1.1 above. Also the frame rate is important to take into consideration, for the same reason.

In the following analysis, eq. 7.8 will be written as

$$G(t) = 1 + p_1 \left(1 - e^{p_2 \cdot t}\right), \quad (7.9)$$

where two new constants are defined as

$$p_1 \equiv D \frac{S}{S + \tau_T/\tau_D}, \quad (7.10)$$

$$p_2 \equiv \frac{S}{\tau_T} + \frac{1}{\tau_D}. \quad (7.11)$$

In order to compare the experimental results to the analytical model, the detector signal from each flood scan was fitted to the gain function in eq. 7.9. The image lag was subtracted prior to the fitting, in order to isolate the gain due to ghosting. The result of many different flood scans was considered, using a variety of experimental parameters and different parts of the detector. Curve fits were performed for each individual result and the best fit constants, p_1 and p_2 , were determined in each case. A few examples of these curve fits are shown in Figure 7.6.

In the next step, the best fit constants, p_1 and p_2 , were plotted as a function of the incoming signal S (or rather, the signal in the first frame of the scan). The model predicts that p_2 should depend linearly on S , while p_2 has a slightly more complex dependence. The resulting best fit constants are shown in Figure 7.7, together with fitted curves, according to eqs. 7.10 and 7.11.

One can immediately see that the results are not perfect fits. This is especially clear in Figure 7.7a, where some of the values of p_1 end up significantly below the expected values. However, the fact that p_1 and p_2 stay fairly close the expected values, for a variety of experimental parameters, strongly indicate that there is some truth behind the model. This will become more apparent, when the model is used to remove the gain effect from the measured images.

The fitting of p_1 and p_2 , to the functions in eqs. 7.10 and 7.11, finally determines the constants C , τ_T and τ_D . The determined values are listed below.

$$\begin{aligned} D &= 0.0332 \\ \tau_T &= 3.01 \cdot 10^6 \text{ (detector signal)} \\ \tau_D &= 25.7 \text{ s} \end{aligned} \quad (7.12)$$

In order to provide reference values for these constants, it should be mentioned that the detector signal values typically ranges up to about $6 \cdot 10^4$ and a typical frame rate is about 10 Hz.

7.4 Correction for Image Lag and Ghosting

The derived models were used in an algorithm, which takes the raw images from any scan and makes corrections for image lag and ghosting. The arguments that

7.4. CORRECTION FOR IMAGE LAG AND GHOSTING

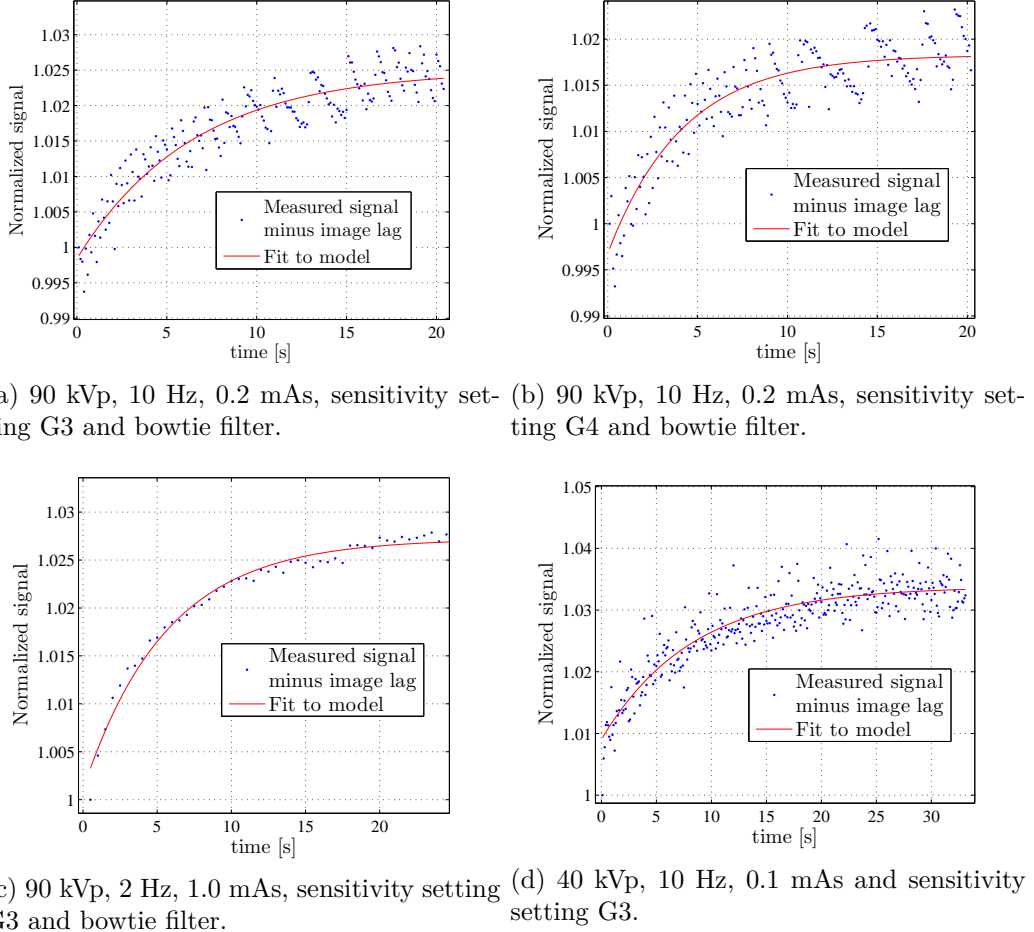
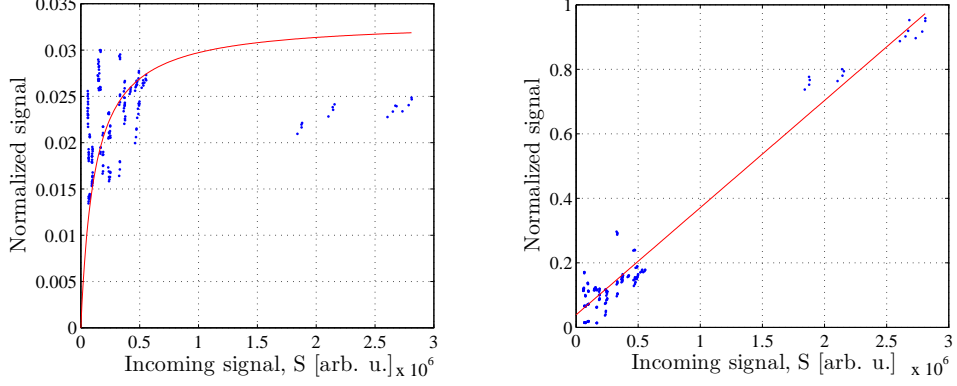


Figure 7.6: Fitting the analytical gain model to experimental data from flood scans. The figure shows a few examples with a range of experimental parameters.

go into this algorithm are, except for the images, the frame rate and the sensitivity setting.

The algorithm was tested on a number of flood scans, of different kVp, mAs and frame rate. The average signal value over different parts of the detector was considered, and plotted as a function of time.

Some results, for a variety of experimental parameters, are shown in Figure 7.8. The plots show the measured signal, the signal after subtracting image lag as well as the final corrected signal, where also ghosting has been removed. The results are meant to be randomly selected, among the many performed scans, in order to give a reliable impression of the performance of the algorithm.

(a) The constant p_1 , as defined in eqs. 7.9 (b) The constant p_2 , as defined in eqs. 7.9Figure 7.7: The experimental constants p_1 and p_2 , as functions of the incoming signal, S . The red lines show curve fits, according to eq. 7.10 and 7.11, respectively.

7.4.1 Practical Implementation of Image Lag Correction

In image correction algorithms for CBCT, computational speed is crucial. The image correction should not take more than a few minutes, in order to be useful in an actual clinical application. When it comes to the correction of image lag, this might lead to complications.

The total image lag originates from all previous images. Using the function $C \cdot t^{-\gamma}$ to describe the transient signal, each image would have to be saved throughout the correction process. This would occupy a lot of memory space and thus slow down the process. Note that this does constitute a problem in the ghosting model, since the contributions from each image are successively added to the gain. A suggested solution to this problem is presented here.

The need to save all previous images, in the image lag correction algorithm, can be avoided by approximating the power function as a sum of decaying exponentials. Assume that we have image lag according to

$$I(t) = I_0(A \cdot e^{-\alpha t} + B \cdot e^{-\beta t}), \quad (7.13)$$

where A , B , α and β are known constants. Now, consider a scan, where the incoming signal in each frame is denoted S_n and the time between each frame is Δt . The total image lag in frame N can be written

$$\begin{aligned} L(N) &= S_1(A \cdot e^{-\alpha \Delta t} + B \cdot e^{-\beta \Delta t}) + \cdots + S_{N-1}(A \cdot e^{-\alpha(N-1)\Delta t} + B \cdot e^{-\beta(N-1)\Delta t}) = \\ &= A(S_1 e^{-\alpha \Delta t} + \cdots + S_{N-1} e^{-\alpha(N-1)\Delta t}) + B(e^{-\beta \Delta t} + \cdots + S_{N-1} e^{-\beta(N-1)\Delta t}) \equiv \\ &= A \cdot L_A(N) + B \cdot L_B(N). \end{aligned} \quad (7.14)$$

In order to obtain the image lag in frame $N + 1$, it is simply a matter of adding signal S_N to the terms $L_A(N)$ and $L_B(N)$, and multiplying by the respective ex-

7.4. CORRECTION FOR IMAGE LAG AND GHOSTING

ponentials. This can be written as

$$\begin{aligned} L_A(N+1) &= (L_A(N) + A \cdot S_N)e^{-\alpha\Delta t}, \\ L_B(N+1) &= (L_B(N) + B \cdot S_N)e^{-\beta\Delta t}. \end{aligned} \quad (7.15)$$

Using this procedure, only the current values of L_A and L_B have to be saved, for each pixel. This will take up the same memory space as two raw images.

A curve fit was made, in order to match a sum of exponential functions to the derived power-law function. The following function gave a result, very close to the power function.

$$I(t) \approx 0.00636 \cdot e^{-t/0.1} + 0.000877 \cdot e^{-t/0.5} + 0.000149 \cdot e^{-t/3} + 0.0000270 \cdot e^{-t/15}. \quad (7.16)$$

Note that four exponential terms means that four values have to be saved, for each pixel, throughout the correction procedure.

The approximation, using four exponential functions was implemented in an algorithm that subtracts the image lag from the images of a scan. The result is shown in Figure 7.9, together with the algorithm that uses the power law model. It can be seen that the approximation, using four exponentials, follows the power-law model perfectly.

7.4.2 Reconstruction after Image Lag and Ghosting Correction

As a final test, an actual reconstruction of a 3D geometry is considered. A scan was made of a Catphan®, a quality assurance phantom used to evaluate the performance of a CT scanner. The raw images were corrected, using the image lag and ghosting correction algorithm, prior to tomographic reconstruction. In Figure 7.10, a section of the phantom is shown, containing attenuating rods of varying size and composition. In order to reduce noise, 40 slices over 2 cm of the phantom, were averaged.

It turns out that the difference between the corrected and uncorrected results is difficult to identify, through visual inspection. This is because the corrected artifacts are submerged by other artifacts, such as noise and scattering. However, the differences can be isolated by subtracting the corrected result from the uncorrected. This is shown in Figure 7.11. Here, one can clearly see a blurring artifact, extending from the attenuating rods in the direction opposite to the direction of rotation. This is a known effect of image lag and ghosting, often referred to as a *comet artifact* [20]. This artifact is reduced by the image lag and ghosting correction algorithm, and is therefore clearly visible in the subtraction image.

CHAPTER 7. RESULTS

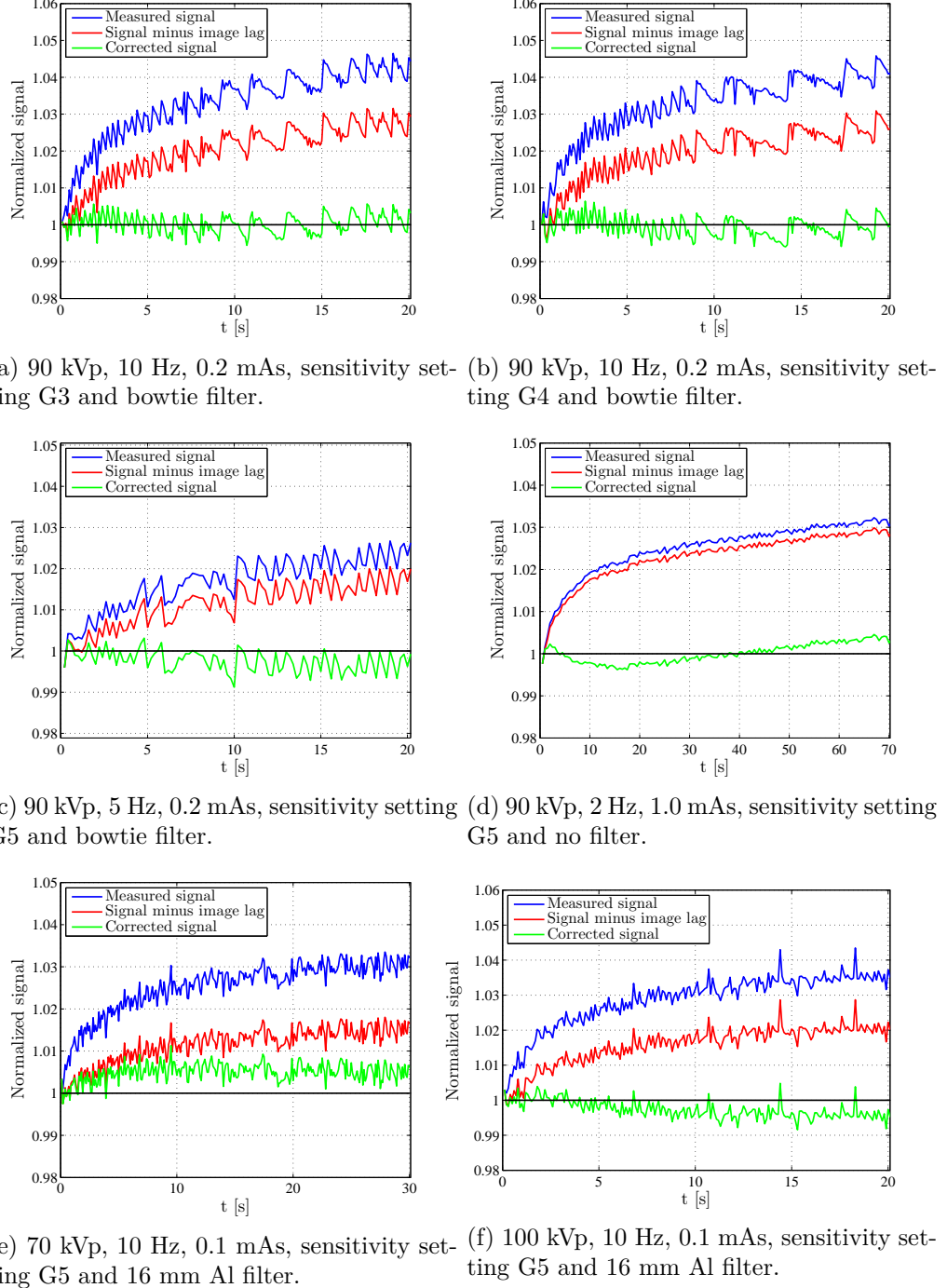


Figure 7.8: A few examples of the correction of the measured detector signal, implementing the derived models of image lag and ghosting. The average signal, over 100×100 pixels, is considered in each case. The experimental parameters are given in the caption of each individual plot.

7.4. CORRECTION FOR IMAGE LAG AND GHOSTING

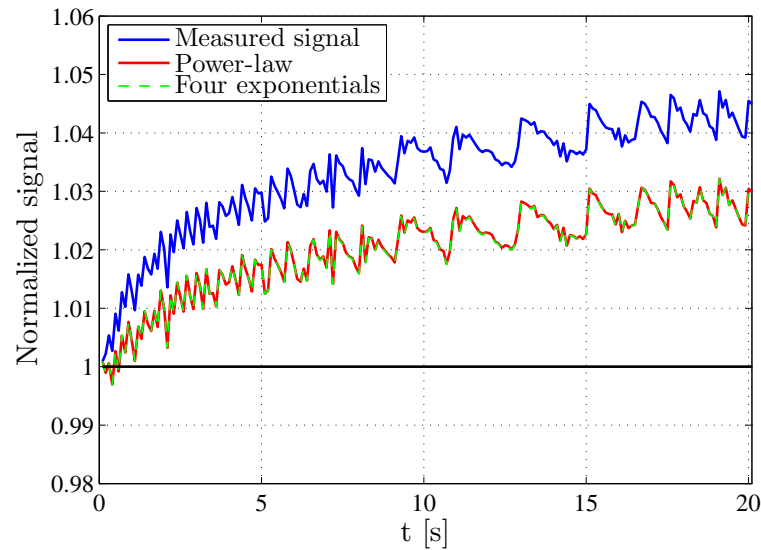


Figure 7.9: A comparison between the power-law model of image lag and the approximation, using four decaying exponentials. It is evident that the approximation gives, close to, equivalent results. The data is from a measurement at 90 kVp, 0.1 mAs and a frame rate of 10 Hz.

CHAPTER 7. RESULTS

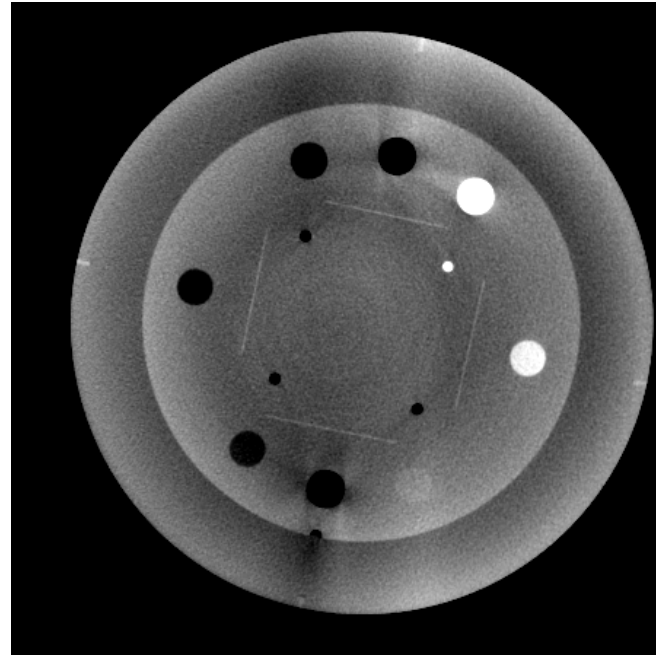


Figure 7.10: A reconstructed tomographic image of the phantom, obtained after applying the image lag and ghosting correction algorithm to the raw images.

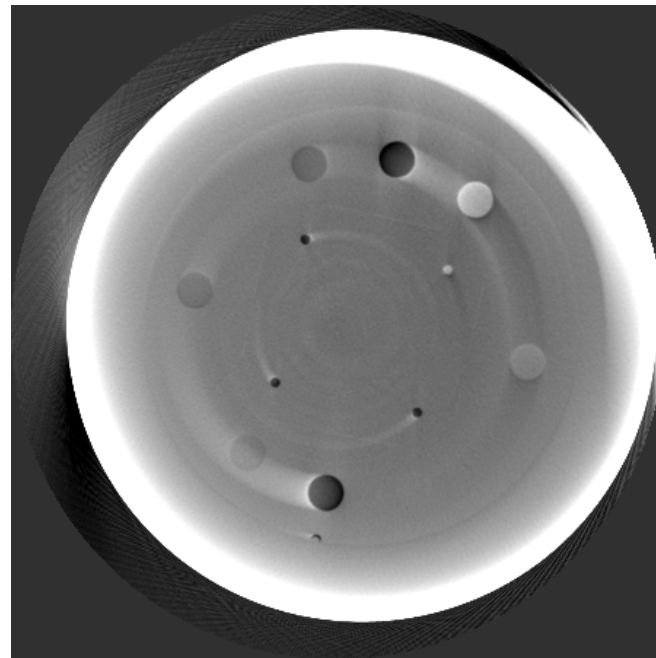


Figure 7.11: A subtraction of the corrected tomographic image from the uncorrected. A blurring artifact is clearly visible, extending from the attenuating rods in the direction opposite to the direction of rotation.

8 | Discussion

Brief discussions and comments were provided together with the results in chapter 7. The results were explained and the comparisons with the derived models were evaluated.

In this chapter, some more detailed discussions are given, concerning mainly the validity of the models and the assumptions made. Furthermore, possible error sources are discussed, as well as potential improvements and future work.

Finally, some notes are presented on the application of the derived models, in image correction algorithms. Since much of the image correction and the tomographic reconstruction lies beyond the scope of this thesis, this discussion will be kept brief.

8.1 The Scintillator Thickness

As discussed in chapter 6, the scintillator thickness could not be accurately determined through experiments. Instead, an approximate thickness had to be used, when determining the PSF. It was estimated partially from technical data from competing manufacturers of flat panel scintillators, and partially from standard values, used in literature.

Because of the generality of the analytical PSF model, it has the ability to (to a certain extent) compensate for inaccurate assumptions [7]. The scintillator thickness is an example of this ability. The spread is not modelled explicitly, but rather assumed to be a function of the absorption depth, z . The fit to experimental results will therefore adjust the model to compensate for the approximative thickness. Similarly, the experimental energy-dependent factor will adjust the model so that it gives a correct absolute output signal.

In the comparison between experimental results and the analytical model, different values of the scintillator thickness were tested and evaluated. The differences between the results, at different thicknesses, were very small and hence, the estimate value of $600 \mu\text{m}$ was kept.

8.2 The Point Spread Function

The model of the PSF could be fitted to the experimental results, with fairly good accuracy. Measurements at different kVp were used to achieve a varying attenuation at different depths, thus providing a more reliable verification of the derived model.

The results in Figure 7.3 show that the model follows the measured result, but slightly underestimates the spread in all three cases. This is especially apparent in the long tails of the edge spread function, measured at 120 kVp.

The error can be assumed to depend mainly on the simplified model. First of all, the depth-dependent spread was assumed to have the same functional form for each z . This is probably not completely true. Nevertheless, this made it possible to reach a simple analytical final expression for the PSF.

Secondly, the absorption of X-rays, and the conversion into optical photons, were assumed to take place in a single point. This was known to be an approximation, since electrons ejected from their bound states, by an incident X-ray photon, or by the so called *Auger effect*, can travel significant distances within the material. This may also be the reason why the tails of the measured edge spread function increased at higher X-ray energies. It would certainly be something worth looking into, if further work to refine the model.

Until the model can be further improved, an underestimation of the spread is preferred. As long as the spread of the response is not exaggerated, it can be taken to be closer to the true PSF than the otherwise assumed delta function response.

8.2.1 The depth-dependent spread

An important part of the PSF is the width of the spread, which was assumed to depend on the depth of absorption. The results presented in Figure 7.2 show that the spread increases with the depth. This may seem unintuitive, since a short way to the active matrix array should mean a narrower spread.

In chapter 3, it was discussed how a reflective backing layer is often used in order to increase the light output of a scintillator. In chapter 4 it was also mentioned that the emission of optical photons, in the scintillator, is isotropic. Some of the optical photons, created deep in the scintillator, will therefore travel all the way to the surface and down again, before being detected. This gives a longer distance travelled and reasonably, a wider spread.

With this argument, it is not unlikely that the spread increases with the absorption depth. Whether the modelled scintillator really has a reflective backing layer has not been confirmed.

8.3 The Temporal Response

Through the experiment, described in section 6.3.2, the image lag could be properly measured and characterized. The results were consistent for a variety of experimental parameters.

8.4. SOME NOTES ON THE EXPERIMENTAL DATA

The ghosting could not be measured with the same accuracy, and hence, a simplified model had to be used to describe this effect. In the results, presented in Figure 7.8, one can see that the ghosting correction does not work perfectly. Sometimes, the algorithm slightly over-corrects or under-corrects the signals from the flood scans. Some scans also show a surprisingly fast increase in signal strength within the first few images, which the algorithm has difficulties to predict. Nevertheless, all considered images from the flood scans are improved by this correction, in the sense that corrected signal comes closer to the expected constant value. Note that if an under-correction is strongly preferred, the value of the derived ghosting constant D , given in eq. 7.12, can be reduced.

The strength of the combined model, of the temporal response, is particularly clear when considering flood scans of different frame rate. As the frame rate decreases, so does the effect of image lag. The gain, due to ghosting, then constitutes a larger part of the total gain, which is accounted for by the model.

8.4 Some Notes on the Experimental Data

All experimental measurements were, to some extent, disturbed by a fluctuating signal. This can be seen in many of the displayed results in chapter 7. The dark current from the detector was measured several times, but the fluctuations exceeded these values by several orders of magnitude. Also the electrical noise sources of the detector are not expected to reach such magnitudes. This leads us to suspect that the pulses, produced by the X-ray tube, are not of equal magnitude. This suspicion is further strengthened by the fact that increasing the pulse time (without increasing the mAs) typically reduces the fluctuations in detector signal.

Throughout the experiments and the comparison with derived models, the ambition was to include all data and avoid the concept of selecting data that matched the expectations. This ambition was generally followed, but two exceptions were made.

The exceptions both concern the fitting of experimental data to the model of ghosting, as described in section 7.3. In some of the measurements, where the incoming X-ray intensity was very low, the detector gave a strongly fluctuating signal along on of its edges. The curve fits to the ghosting model could not be performed, and consequently this part of the detector was not included for a few measurements.

In the other case, a very high X-ray intensity resulted in an additional gain, which continued to increase the signal, where the other measurements would flatten out. This additional gain was not used in the determination of the constants of the ghosting model. A possible explanation to the extra gain may be an increased temperature, due to the high exposure. It may be of interest to investigate this effect in the future.

Nevertheless, the models of image lag and ghosting showed to correct even these cases, with satisfactory results.

8.5 Image Correction

The derived models of the spatial and temporal response of the detector can be used in image correction algorithms, in order to improve the quality of the CBCT. A brief overview of the current work in this field, at Elekta, was given in chapter 1.

Some corrections were already performed and the results were presented in Chapter 7. In addition to the flood scans, already discussed above, a tomographic reconstruction of a phantom was considered. The results showed that the correction algorithm reduces artifacts, directly related to the temporal characteristics of the detector. However, other artifacts and noise were found to surpass these extent of these artifacts, and the improvements could not be seen by visual inspection of the tomographic images. It is hoped that some of the other artifacts, present in the reconstructed images, can be removed using applications that are currently under development.

9 | Conclusion

A physical model was developed, characterizing the response of a Thales Pixum CBCT 2630 X-ray detector. The model takes into account both the spread of the signal, across adjacent pixels, and the temporal characteristics, causing residue images in subsequent projections as well as a change in sensitivity due to previous exposure.

The spatial response was described by the energy- and angle-dependent point spread function, $PSF(x, y, \theta, \phi, E)$. The model assumes an exponential shape of the response, with a width that depends linearly on the depth of absorption. The energy dependence enters through the energy-dependent attenuation in the CsI:Tl scintillator. The response from a single X-ray absorption event was assumed to be symmetric, however, the total response will be asymmetric at any finite incident angle.

Measurements were made of the signal across a sharp edge, the so called edge spread function. By comparing the experimental results to the analytically derived model, the depth-dependent width was determined. Experiments at 50, 90 and 120 kVp gave fairly coinciding results and the final result was chosen such as to slightly underestimate the width of the response.

An energy dependent factor was also added to the model, in order to match the measured response signal values. The final expression for the derived PSF was

$$PSF_{Mod}(x, y, \theta, \phi, E) = \int_0^{z_{max}} \mu_{PE}(E)E \exp\left(-\frac{\mu_{tot}(E)z}{\cos\theta}\right) (1 + a_1E) \frac{\exp\left(-\frac{\sqrt{(x-z\tan\theta\cos\phi)^2+(y-z\tan\theta\sin\phi)^2}}{g_0+g_1z}\right)}{(g_0+g_1z)^2} dz, \quad (9.1)$$

where $\mu_{tot}(E)$ and $\mu_{PE}(E)$ are the total and the photoelectric attenuation constants of CsI. All determined constants are tabulated in the end of this chapter.

The temporal detector response is characterized by two closely related phenomena, here referred to as image lag and ghosting. Image lag is the residual signal, from previous X-ray exposures, that is carried over into subsequent image frames. Ghosting, on the other hand, is the change in detector sensitivity, as a result of previous exposure. It is likely that both effects are due to charge trapping the in a-Si:H photodiodes.

CHAPTER 9. CONCLUSION

Through a series of experiments, the temporal effects were measured and individually characterized. The image lag signal was shown to decay with time according to

$$I(t) = S_0 \cdot C t^{-\gamma}, \quad (9.2)$$

where $I(t)$ is the detected signal and S_0 is the incoming signal at $t = 0$. (See table 9.1 for coefficient values.) This result agrees with the theoretical and experimental prediction by Scher and Montroll from 1975 [18].

Ghosting had not been as well described as image lag, and therefore, a new physical model was developed. This, somewhat simplified, model is based on the time-dependent trapping and detrapping of charge in the a-Si:H photodiodes. Through comparisons with a number of flood scans, after first subtracting the image lag, the trapping and detrapping constants were determined.

The ghosting model describes the fraction of occupied trapped states, $n(t)$, in the photodiode as

$$\frac{dn(t)}{dt} = \frac{S(t)}{\tau_T} (1 - n(t)) - \frac{n(t)}{\tau_D}, \quad (9.3)$$

where $S(t)$ is the incoming signal intensity at time t . It is important to note that $S(t)$ is the signal value per second, at detector sensitivity setting G3. When using sensitivity setting G4 and G5, the values should be divided by the factors 0.224 and 0.165, respectively. It should also be mentioned that the detector signal value typically ranges up to about $6 \cdot 10^4$.

After obtaining the occupation of trapped states, the sensitivity gain can then be calculated according to

$$G(t) = 1 + D \cdot n(t). \quad (9.4)$$

Finally, an image correction algorithm was written, which subtracts the effects of image lag and ghosting from any scan sequence. The algorithm was tested on a multiple flood scans, with a range of experimental parameters, as well as on a scan of a 3D phantom. The results were overall successful.

The models derived in this thesis may be further used in the image correction applications, currently under development at Elekta. The goal is to improve the quality of the CBCT, to give better soft tissue contrast. This may extend the possible use of the CBCT system, beyond its primary application in patient positioning.

Constant	Value	Unit	C	$2.53 \cdot 10^{-4}$	$s^{1.11}$ (*)
z_{max}	600	μm	γ	1.11	-
a_1	0.0331	keV^{-1}	τ_T	$3.01 \cdot 10^6$	detector signal
g_0	80	μm	τ_D	25.7	s
g_1	0.35	-	D	0.0332	-

Table 9.1: Table of derived constant. (*) See discussion in Section 7.2.3

Bibliography

- [1] J Adler. GPU Monte Carlo scatter calculations for Cone Beam Computed Tomography. Master's thesis, KTH Royal Institute of Technology, 2014.
- [2] L Antonuk et al. Radiation response characteristics of amorphous silicon arrays for megavolt radiation imaging. *IEEE Trans Nucl. Sci.*, 1992.
- [3] A Badano and J Sempau. MANTIS: combined x-ray, electron and optical Monte Carlo simulations of indirect radiation imaging system. *Phys. Med. Biol.*, 2006.
- [4] J Bearden and A Burr. Reevaluation of X-ray Atomic Energy Levels. *Rev. Mod. Phys.*, 1967.
- [5] J Beurel, H Kundel, and R Van Metter. *Medical Imaging, Volume 1. Physics and Psychophysics*. SPIE, 2000.
- [6] M Born and E Wolf. *Principles of optics, 3rd revised edition*. Oxford: Pergamon Press, 1965.
- [7] M Freed, S Park, and A Badano. A fast, angle-dependent, analytical model of CsI detector response for optimization of 3D x-ray breast imaging systems. *Med. Phys.*, 2010.
- [8] I Fujieda et al. High Sensitivity Readout of 2D a-Si Image Sensors. *Jpn. J. Appl. Phys.*, 1993.
- [9] R Gwin and R Murray. Scintillation process in CsI(Tl). II Emission spectra and the possible role of self-trapped holes. *Phys. Rev.*, 1963.
- [10] K Hecht. Zum Mechanismus des lichtelektrischen Primärstromes in isolierenden Kristallen. *Z. Physik*, 1932.
- [11] G Knoll. *Radiation Detection and Measurement*. John Wiley and Sons, Inc., 1999.
- [12] N Mail, D Moseley, J Siewerdsen, and D Jaffray. An empirical method for lag correction in cone-beam CT. *J. Appl. Clin. Med. Phys.*, 2008.

BIBLIOGRAPHY

- [13] N Mail, N O'Brien, and G Pang. Lag correction model and ghosting analysis for an indirect-conversion flat-panel imager. *J. Appl. Clin. Med. Phys.*, 2007.
- [14] OECD Nuclear Energy Agency (NEA). *PENELOPE-2011 : A Code System for Monte Carlo Simulation of Electron and Photon Transport*, 2011.
- [15] M Overdick et al. Temporal Artefacts in Flat Dynamic X-ray Detectors. *Proc. SPIE*, 2001.
- [16] PerkinElmer. Dexela flat panel cmos x-ray detectors, May 2014. [online] <http://www.dexela.com/cmos.aspx>.
- [17] Hamamatsu Photonics. Scintillator plates, May 2014. [online] <http://www.hamamatsu.com/jp/en/product/category/3100/3010/index.html>.
- [18] H Scher and E Montrol. Anomalous transit-time dispersion in amorphous solids. *Phys. Rev. B*, 1975.
- [19] J Siewersen and D Jaffray. A ghost story: spatio-temporal response characteristics of an indirect-detection flat-panel imager. *Med. Phys.*, 1999.
- [20] J Siewersen and D Jaffray. Cone-beam computed tomography with a flat-panel imager: effects of image lag. *Med. Phys.*, 1999.
- [21] J Siewersen, A Waese, S Richard, and D Jaffray. Spektr: A computational tool for x-ray spectral analysis and imaging system optimization. *Med. Phys.*, 2004.
- [22] J Starman, J Star-Lack, G Virshup, E Shapiro, and R Fahrig. A nonlinear lag correction algorithm for a-Si flat-panel x-ray detectors. *Med. Phys.*, 2012.
- [23] J Starman, C Tognina, L Partain, and R Fahrig. A forward bias method for lag correction of an a-Si flat panel detector. *Med. Phys.*, 2012.
- [24] R Street. *Hydrogenated Amorphous Silicon*. Cambridge University Press, 1991.
- [25] W Strehlow and E Cook. Compilation of Energy Band Gaps in Elemental and Binary Compound Semiconductors and Insulators. *J. Phys. Chem. Ref. Data.*, 1973.
- [26] T Tiedje and A Rose. A physical interpretation of dispersive transport in disordered semiconductors. *Solid State Communications*, 1980.
- [27] J Valentine, W Moses, S Derenzo, D Wehe, and G Knoll. Temperature dependence of CsI(Tl) gamma-ray excited scintillation characteristics. *Trans. Nucl. Sci.*, 1993.
- [28] H Wieczorek. Effects of Trapping in a-Si:H Diodes. *Solid State Phen.*, 1995.

BIBLIOGRAPHY

- [29] XCOM: Photon Cross Sections Database , April 2014. [online] <http://www.nist.gov/pml/data/xcom/index.cfm>.
- [30] K Zanio, W Akutagawa, and R Kikuchi. Transient Currents in SemiInsulating CdTe Characteristic of Deep Traps. *J. Appl. Phys.*, 1968.
- [31] W Zhao et al. Ghosting caused by bulk charge trapping in direct conversion flat-panel detectors using amorphous selenium. *Med. Phys.*, 2008.